Inertial wave singularities from two-dimensional tips and wedges

By Stéphane LE DIZÈS & Benjamin FAVIER

Aix Marseille Université, CNRS, Centrale Méditerranée, IRPHE, Marseille, France

(Received 26 May 2026)

This study examines the structure of the inertial wave field generated by small harmonic oscillations of a two-dimensional wedge in an unbounded, uniformly rotating fluid. We demonstrate that inviscid singularities generically emerge in the form of singular eigenmodes satisfying homogeneous boundary conditions and outgoing wave conditions. These modes produce velocity fields that behaves as $|x_\perp|^{\alpha-1}$ along the rays emanating from the wedge apex, where $x_\perp$ denotes the distance from the critical line. The complex exponents α are determined by a simple discrete relation depending only on wedge geometry and wave propagation angle. For inviscid forcing, the exponent is selected by finite-energy constraints ($\Re e(\alpha) \geq 1/2$). A viscous approximation is then constructed by extending classical self-similar solutions to complex exponents, capturing the internal structure and evolution of the wave beam. Higher-order corrections enforcing no-slip boundary conditions are also derived. For viscous forcing, the boundary layer flow induces a tangential mismatch that is balanced by radial flux in the bulk, thereby fully prescribing the amplitude of the only singular eigenmode with radial flux (the Dirac eigenmode with $\alpha = 0$). The theory is validated through direct numerical simulations for both inviscid and viscous forcing, showing excellent agreement in both unbounded and bounded configurations. Finally, the framework suggests broader implications, including wave scattering by sharp edges, extensions to three-dimensional geometries, and potential explanations for edge-emitted sheet-like structures observed in librating or precessing titled cubes.

1. Introduction

Rotating and stratified fluids have the ability to support wave motion. The main characteristic of these waves (inertial waves in rotating fluids and internal gravity waves in stratified fluids) is that they propagate in directions that make a constant angle with respect to the axis of rotation or the direction of stratification. In a rotating fluid, this angle φ only depends on the wave frequency through the relation $\omega = 2\Omega \sin\varphi$ where Ω is the rotation rate of the medium. These propagation directions correspond to the characteristics of the wave equation satisfied by these waves in an inviscid fluid. It is along these directions that any singular feature of a harmonic field will be transported within the fluid. In the present study, we are concerned with the singularities associated with an oscillating two-dimensional boundary that exhibits a geometric singularity in a rotating medium. More precisely, our objective is to characterise the linear wave field generated by a two-dimensional wedge, that is, a discontinuity in the slope of the fluid boundary.

The first studies on the effect of a wedge in stratified fluids arose in the context of scattering problems. The central question was how the classical reflection law for a plane

internal wave incident on a planar boundary (Phillips, 1966) is modified when a wedge is present. Among the relevant works, we may cite Robinson (1969, 1970), Wunsch (1968, 1969), and Hurley (1970). The latter was probably the first to present the inviscid singular solution that we shall re-derive below. Its derivation is based, as we shall see, on the careful application of the radiation condition (Mowbray & Rarity, 1967; Baines, 1971; Lighthill, 1978). The scattering results by Robinson (1969) were adapted to the problem of wave generation by a barotropic tide over sharp-edged topography by St Laurent *et al.* (2003) and Llewellyn Smith & Young (2003), and used to estimate the energy conversion rate when the Weak Topography Approximation (Bell, 1975) does not apply .

Additional results were obtained using boundary-integral methods (Voisin, 2021). Hurley (1997) derived the expression for the inviscid wave field generated by an oscillating elliptical cylinder. When one of the ellipse's semi-axis tends to zero, this solution provides the wave field induced by an oscillating ribbon. The viscous generation of waves for this geometry was also considered by Kistovich & Chashechkin (1999) using a different approach. This approach was extended, using Hankel transforms, to the disc, both for an inviscid fluid (Martin & Llewellyn Smith, 2011; Il'inyhk & Chashechkin, 2004; Bardakov *et al.*, 2007) and for a viscous fluid (Tanzosh & Stone, 1995; Davis & Llewellyn Smith, 2010; Le Dizès, 2015). In all these cases, the dominant feature of the wave field is the intense wave beam originating from the edge of the disc or ribbon.

Intense thin beams are also observed to be emitted from corners in closed cavities. Experimental observations have been reported in cylinders (McEwan, 1970), frustums (Klein *et al.*, 2014) and cubes (Boisson *et al.*, 2012). These beams seem to be particularly visible when those emitted from two different wedges connect, which occurs at specific frequencies. In the frustum, as well as in 2D trapezoidal tanks, the wave field may also converge onto an attractor (Maas *et al.*, 1997). Depending on the frequency, this attractor is either a curve within the bulk of the fluid or the apex of one wedge of the container. This first case, which also corresponds to an inviscid singularity in the bulk, will not be our concern here. Our analysis will, however, provide some information on the structure of the wave field in the second case. This situation corresponds to a geometry initially discussed by Greenspan (1969), and later considered experimentally in Beardsley (1970) and theoretically in Troitskaya (2010).

In three-dimensional angular domains, such as a tilted cube, waves emitted from vertices and edges appear to play a central role in structuring the complex response generated by libration or precession, as observed in numerical simulations (Wu *et al.*, 2020, 2022, 2024). While Wu *et al.* (2020, 2022) proposed distinct rules for determining the propagation direction of waves emitted from edges, our results will provide a unified explanation for both the dominance of wedge beams and the selection of their propagation direction.

As we shall see, the singularities created by wedges share many similarities with critical-slope singularities (Greenspan, 1968; Kerswell, 1995; Le Dizès & Le Bars, 2017; Le Dizès, 2024). These singularities occur when the boundary is tangent to one of the propagation directions. They manifest as intense thin beams emitted from the critical points of the boundary. Le Dizès (2024) showed that they are associated with an underlying inviscid singularity of the velocity field in $|x_\perp|^{-5/4}$ for a viscous forcing and in $|x_\perp|^{-1/2}$ for an inviscid forcing, where $x_\perp$ denotes the distance to the critical line. The wedge-induced singularities will be shown to be of the form $|x_\perp|^{\alpha-1}$ where α is a complex number depending on the wedge and propagation angles.

As for the critical-slope singularities, wedge-induced inviscid singularities are smoothed by viscosity (Le Dizès, 2024). This regularizing process is now well established. It occurs over a width of order $E^{1/3}$ and is described by the similarity solutions first introduced by Moore & Saffman (1969) and Thomas & Stevenson (1972). Using these approximations,

we will be able to compare our theoretical predictions for wedge-induced singularities with direct numerical simulations of oscillating wedges.

The paper is organised as follows. In section §2, we present the general framework. The geometry, the local coordinate system, the governing equations and the boundary conditions are introduced. In section §3, we focus on the inviscid analysis and explain how the radiation conditions are implemented on singular fields. We show that the inviscid solution near the apex of the wedge consists of a forced response and (possibly) singular eigenmodes with specific properties. In this section, the possible values of the singularity exponent α are derived. Among the possible singular eigenmodes, we recover the Dirac solution corresponding to a source/sink placed at the apex with an exponent $\alpha = 0$. In section §4, we consider viscous effects. We first explain how the singular inviscid solutions are smoothed by viscosity using the similarity solutions of Moore & Saffman (1969) and Thomas & Stevenson (1972). We then examine the case of a viscous forcing and show how the Dirac solution may be excited to balance the flux generated along the wedge in the viscous boundary layers. Finally, we compute the viscous corrections obtained by applying no-slip boundary conditions on the inviscid solutions. In particular, we show that this correction is more singular than the singular solution that generated it. Section §5 deals with direct numerical simulations in two different geometries (a square in an infinite domain and the flow within a triangle) with both viscous and inviscid forcing. The numerical solutions are compared with the asymptotic expressions obtained near the apex of the different wedges. Section §6 discusses possible extensions of the results while the last section summarises the main findings.

2. Framework

We consider an incompressible fluid with kinematic viscosity ν uniformly rotating at a constant angular velocity Ω around the axis $\mathbf{e}_\Omega$. We are interested in the perturbations generated in an unbounded domain by the small harmonic displacements of the boundary of a two-dimensional object featuring a wedge or a tip at the origin O. The object, which is invariant along the Oy axis, has a typical cross-sectional size L. It is defined by its contour $\mathcal{C}$ in the cross-section. An example of such an object is illustrated in figure 1(a). Note that while the figure shows the particular case of an acute wedge angle, our results are valid for all cases including obtuse angles. We define the Oz axis as the projection of the vector $\mathbf{e}_\Omega$ onto the plane perpendicular to the Oy axis and denote by β ($-\pi/2 < \beta < \pi/2$) the angle between the vector $\mathbf{e}_\Omega$ and the Oz axis [see figure 1(a)].

The displacements are assumed to be sufficiently small such that a linear approach can be used. In this limit, the object boundary $\mathcal{S}$ can be considered as fixed and the fluid subject to a prescribed velocity $\epsilon\mathbf{V}(x,z)e^{-\mathrm{i}\omega t} + c.c.$ on this boundary, where ω is the frequency. Normalizing the perturbations by the displacement amplitude ϵ, we can reduce the governing equations to the linear system

$$\frac{\partial \mathbf{U}}{\partial t} + 2\Omega\, \mathbf{e}_\Omega \times \mathbf{U} = -\nabla P + \nu \Delta \mathbf{U}, \tag{2.1a}$$

$$\nabla \cdot \mathbf{U} = 0. \tag{2.1b}$$

with the boundary conditions

$$\mathbf{U}(\mathbf{x}) = \mathbf{V}(x,z)e^{-\mathrm{i}\omega t} + c.c. \quad \text{for} \quad \mathbf{x} \in \mathcal{S} \tag{2.2a}$$

$$\mathbf{U}(\mathbf{x}) \to 0 \quad \text{as} \quad x^2 + z^2 \to \infty. \tag{2.2b}$$

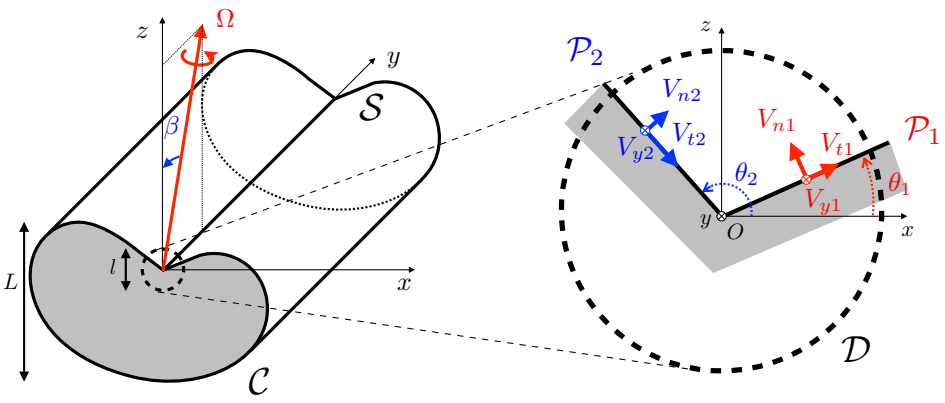

FIGURE 1. (Left) Example of 2D geometry with a wedge in a rotating fluid. (Right) Close-up view on the wedge in the (x,z) plane. Definition of the parameters of the local problem.

We focus on the synchronized fluid response which can be written in the form

$$(\mathbf{U},P)=(\mathbf{u},p)e^{-\mathrm{i}\omega t}+c.c.$$

where the amplitudes $\mathbf{u}$ and p are independent of the y-coordinate, in accordance with the symmetry of the forcing and geometry.

The Coriolis parameter that characterises the inertial waves invariant along the Oy axis, is defined by $f=2\Omega\cos\beta$. We assume that the frequency ω is in the inertial range $0<\omega<f$ and define the angle θ_c $(0<\theta_c<\pi/2)$ such that

$$\omega=f\cos\theta_c. \tag{2.3}$$

If one uses L and f as characteristic scales, the velocity and pressure amplitudes of the harmonic perturbation satisfy

$$-\mathrm{i}\cos\theta_c\,u_x-u_y+\tan\beta\,u_z=-\frac{\partial p}{\partial x}+E\left(\frac{\partial^2}{\partial x^2}+\frac{\partial^2}{\partial z^2}\right)u_x, \tag{2.4a}$$

$$-\mathrm{i}\cos\theta_c\,u_y+u_x=E\left(\frac{\partial^2}{\partial x^2}+\frac{\partial^2}{\partial z^2}\right)u_y, \tag{2.4b}$$

$$-\mathrm{i}\cos\theta_c\,u_z-\tan\beta\,u_x=-\frac{\partial p}{\partial z}+E\left(\frac{\partial^2}{\partial x^2}+\frac{\partial^2}{\partial z^2}\right)u_z, \tag{2.4c}$$

$$\frac{\partial u_x}{\partial x}+\frac{\partial u_z}{\partial z}=0, \tag{2.4d}$$

and the boundary conditions

$$\mathbf{u}(x,z)=\mathbf{V}(x,z)\quad\text{for}\quad(x,z)\in\mathcal{C} \tag{2.5a}$$

$$\mathbf{u}(z,z)\to 0\quad\text{as}\quad x^2+z^2\to\infty. \tag{2.5b}$$

where E the Ekman number defined by

$$E=\frac{\nu}{fL^2}. \tag{2.6}$$

We further assume the existence of a (possibly small) domain $\mathcal{D}$ of cross-sectional size $l\le L$, where the wedge is locally described by the two half-planes $\mathcal{P}_1$ and $\mathcal{P}_2$ oriented at latitudinal angles θ_1 and θ_2 (measured from the Ox axis) and in which the boundary

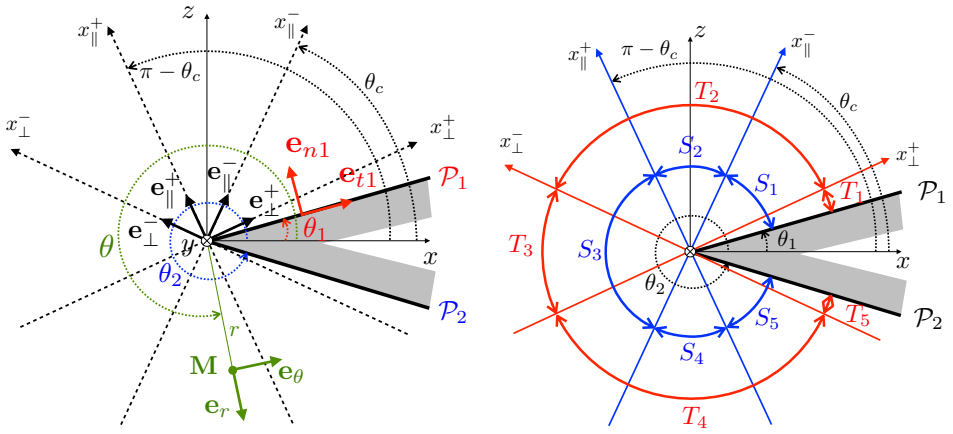

FIGURE 2. (a) Various frames used to describe the solutions. (b) Sectors S_j and T_j where the inviscid solutions and the viscous approximations are uniformly valid. The sectors S_j, $j=1,..,5$ are delimited by the boundaries and the lines $x_\perp^\pm=0$. The sectors T_j, $j=1,..,5$ are delimited by the boundaries and the lines $x_\parallel^\pm=0$. They are labelled in anti-clockwise order from $\mathcal{P}_1$.

condition (2.5a) reduces to

$$\mathbf{u}((x,z)\in\mathcal{P}_1)=\mathbf{V}_1\quad,\quad\mathbf{u}((x,z)\in\mathcal{P}_2)=\mathbf{V}_2, \tag{2.7}$$

where $\mathbf{V}_1$ and $\mathbf{V}_2$ are constant (prescribed) vectors.

The objective of the theoretical works that is presented in the next two sections is to obtain information on the possible solutions in the domain $\mathcal{D}$. For this purpose, we introduce the coordinates $x_\perp^\pm$ and $x_\parallel^\pm$ and unit vectors $\mathbf{e}_\perp^\pm$ and $\mathbf{e}_\parallel^\pm$ defined by

$$x_\perp^\pm=\pm\sin\theta_c x+\cos\theta_c z\ ,\quad x_\parallel^\pm=\mp\cos\theta_c x+\sin\theta_c z\ , \tag{2.8a}$$

$$\mathbf{e}_\perp^\pm=\pm\sin\theta_c\mathbf{e}_x+\cos\theta_c\mathbf{e}_z\ ,\quad \mathbf{e}_\parallel^\pm=\mp\cos\theta_c\mathbf{e}_x+\sin\theta_c\mathbf{e}_z\ , \tag{2.8b}$$

that will be used to describe the solutions in the following sections [see figure 2(a)]. The vectors $\mathbf{e}_\parallel^\pm$ will give the direction of propagation of the singular beams, while $x_\perp^\pm$ will measure the distance to the singularity lines. We also define in figure 2(b) the angular sectors S_j and T_j delimited by the lines $x_\perp^\pm=0$ and $x_\parallel^\pm=0$ that will be used later. In terms of $x_\perp^\pm$, the planes $\mathcal{P}_1$ and $\mathcal{P}_2$ are defined respectively by

$$\mathcal{P}_1:\ x_\perp^-=K_1x_\perp^+\quad,\quad\mathcal{P}_2:\ x_\perp^-=K_2x_\perp^+ \tag{2.9}$$

where

$$K_1=\frac{\sin(\theta_1-\theta_c)}{\sin(\theta_1+\theta_c)}\ ,\quad K_2=\frac{\sin(\theta_2-\theta_c)}{\sin(\theta_2+\theta_c)}. \tag{2.10}$$

We are interested in the weak-viscosity limit $E\to0$. Accordingly, we first consider the inviscid problem ($E=0$, see section 3) before analyzing the viscous case ($E>0$, see section 4).

3. Inviscid analysis

Let us first focus on the inviscid limit by taking $E = 0$. If we introduce the stream-function $\Psi(x, z)$ to describe the flow in the (x, z) plane

$$u_x = \frac{\partial \Psi}{\partial z} \ , \quad u_z = -\frac{\partial \Psi}{\partial x} \ , \tag{3.1}$$

we can reduce the inviscid version of equations (2.4a-d) to

$$\cos^2\theta_c \left(\frac{\partial^2}{\partial x^2} + \frac{\partial^2}{\partial z^2} \right) \Psi - \frac{\partial^2 \Psi}{\partial z^2} = 0 \ . \tag{3.2}$$

From Ψ, we can also get the third velocity component using

$$u_y = -\frac{\mathrm{i}}{\cos\theta_c} \frac{\partial \Psi}{\partial z} \ . \tag{3.3}$$

The general solution to (3.2) can be written as

$$\Psi = \Psi^-(x_\perp^-) + \Psi^+(x_\perp^+) \ , \tag{3.4}$$

and the velocity field in the (x, z) plane becomes

$$\mathbf{u}_{(x,z)} = u_\parallel^-(x_\perp^-)\mathbf{e}_\parallel^- + u_\parallel^+(x_\perp^+)\mathbf{e}_\parallel^+ \ , \tag{3.5}$$

with

$$u_\parallel^-(x_\perp^-) = \frac{d\Psi^-}{dx_\perp^-} \ , \quad u_\parallel^+(x_\perp^+) = -\frac{d\Psi^+}{dx_\perp^+}. \tag{3.6}$$

The transverse velocity u_y is then related to $\Psi^\pm$ and $u_\parallel^\pm$ by

$$u_y = -\mathrm{i}\left(\frac{d\Psi^+}{dx_\perp^+} + \frac{d\Psi^-}{dx_\perp^-} \right) = \mathrm{i}(u_\parallel^+ - u_\parallel^-). \tag{3.7}$$

In the inviscid problem ($E = 0$), only the boundary condition on the normal velocity is applied on $\mathcal{P}_1$ and $\mathcal{P}_2$:

$$\mathbf{u}(\theta = \theta_1) \cdot \mathbf{e}_{n1} = V_{n1} \ ; \qquad \mathbf{u}(\theta = \theta_2) \cdot \mathbf{e}_{n2} = V_{n2}. \tag{3.8}$$

Singular solutions are expected owing to the presence of a singularity in the fluid domain at the origin. These solutions should nevertheless satisfy adequate boundary conditions away from the origin.

3.1. *Boundary conditions on singular fields*

We are interested in configurations where the flow generated by the singularity is not influenced by the external domain. In such cases, no signal should come from the external region, which means that nothing should come from "infinity" in our local domain $\mathcal{D}$. Therefore, the conditions away from the origin should correspond to those in an unbounded (infinite) domain. They can be justified by several arguments.

First, the solution should be composed of waves propagating outward, with their group velocity oriented away from the singularity (Mowbray & Rarity, 1967). This is the argument used in Le Dizès (2024) to derive constraints on singular fields of the form $|x_\perp|^\alpha$. Second, a radiation condition can be derived from causality, by imposing analytic continuation (Lighthill, 1978). If a small positive growth rate is added to the frequency, i. e. $\omega \to \omega + \mathrm{i}0^+$, then the solution should become analytic in the (x, z) plane (Hurley, 1972). This requirement determines the position of the branch cut associated with the singularities (now displaced into the complex plane) and prescribes how they must be

analytically continued. Third, one may argue that the solution should arise as the limit of a viscous solution as the viscosity tends to zero.

Since the origin is the only singular point, the singularities of the solution are expected to lie along the characteristics issued from this point. These characteristics correspond to the lines $x_\perp^+ = 0$ and $x_\perp^- = 0$, shown in figure 2. As shown in Le Dizès (2024), the group velocity argument implies that if a wave propagating in the direction of $x_\parallel^+ > 0$ has a singular behavior of the form $|x_\perp^+|^a$ on one side of the line $x_\perp^+ = 0$, its behavior is prescribed on the other side. More precrisely,

$$\begin{aligned} &\text{If} \qquad u_\parallel^+ \sim A|x_\perp^+|^a \qquad \text{for} \;\; x_\perp^+ > 0 \;\; \text{as} \;\; x_\perp^+ \to 0, \\ &\text{then} \qquad u_\parallel^+ \sim Ae^{\mathrm{i}\pi a}|x_\perp^+|^a \qquad \text{for} \;\; x_\perp^+ < 0 \;\; \text{as} \;\; x_\perp^+ \to 0. \end{aligned} \tag{3.9}$$

This result was established for any non-integer real value of a in Le Dizès (2024). The analyticity argument extends this condition to complex values of a. Indeed, applying the shift $\omega \to \omega + \mathrm{i}0^+$ moves the characteristic line issued from 0 in the direction $x_\parallel^+ > 0$ into the lower half of the complex plane. The corresponding analytic continuation must then occur in the upper complex half-plane, which implies that $x_\perp^+ = |x_\perp^+|e^{\mathrm{i}\pi}$ for negative $x_\perp^+$, thus explaining the factor in $e^{\mathrm{i}\pi a}$ in the expression above for $x_\perp^+ < 0$. The same argument can be used to show that, for a logarithm singularity, the wave propagating in the direction of $x_\parallel^+ > 0$ must satisfy

$$\begin{aligned} &\text{If} \qquad u_\parallel^+ \sim A\log|x_\perp^+| \qquad \text{for} \;\; x_\perp^+ > 0 \;\; \text{as} \;\; x_\perp^+ \to 0, \\ &\text{then} \qquad u_\parallel^+ \sim A(\log|x_\perp^+| + \mathrm{i}\pi) \qquad \text{for} \;\; x_\perp^+ < 0 \;\; \text{as} \;\; x_\perp^+ \to 0. \end{aligned} \tag{3.10}$$

Similar relations are obtained for other quantities. For instance, for the streamfunction Ψ^+ describing the wave propagating in the direction of $x_\parallel^+ > 0$, we have

$$\begin{aligned} &\text{If} \qquad \Psi^+ \sim A|x_\perp^+|^a \qquad \text{for} \;\; x_\perp^+ > 0 \;\; \text{as} \;\; x_\perp^+ \to 0, \\ &\text{then} \qquad \Psi^+ \sim Ae^{\mathrm{i}\pi a}|x_\perp^+|^a \qquad \text{for} \;\; x_\perp^+ < 0 \;\; \text{as} \;\; x_\perp^+ \to 0. \end{aligned} \tag{3.11}$$

These conditions will be used to continue a singular solution from one sector S_j to the neighbouring sectors S_{j-1} and S_{j+1}.

3.2. *Regular inviscid forced response*

With the variables $x_\perp^\pm$, the boundary conditions (3.8) become

$$-\sin(\theta_1-\theta_c)u_\parallel^-(x_\perp^-) + \sin(\theta_1+\theta_c)u_\parallel^+(x_\perp^+) = V_{n1} \;\; \text{for} \;\; (x_\perp^-, x_\perp^+) \in \mathcal{P}_1 \;, \tag{3.12a}$$

$$\sin(\theta_2-\theta_c)u_\parallel^-(x_\perp^-) - \sin(\theta_2+\theta_c)u_\parallel^+(x_\perp^+) = V_{n2} \;, \;\; \text{for} \;\; (x_\perp^-, x_\perp^+) \in \mathcal{P}_2 \;. \tag{3.12b}$$

If $\sin(\theta_2-\theta_1) \neq 0$, the above system admits a simple uniform solution whatever V_{n1} and V_{n2} which is

$$u_\parallel^- = \frac{\sin(\theta_2+\theta_c)V_{n1} + \sin(\theta_1+\theta_c)V_{n2}}{2\sin\theta_c\cos\theta_c\sin(\theta_2-\theta_1)} \;, \tag{3.13a}$$

$$u_\parallel^+ = \frac{\sin(\theta_2-\theta_c)V_{n1} + \sin(\theta_1-\theta_c)V_{n2}}{2\sin\theta_c\cos\theta_c\sin(\theta_2-\theta_1)} \;. \tag{3.13b}$$

For these values of $u_\parallel^+$ and $u_\parallel^-$, equations (3.12a,b) are valid everywhere, so in particular on $\mathcal{P}_1$ and $\mathcal{P}_2$. We shall denote this solution as the regular forced response.

The first point to note is that no such regular response a priori exists if $\sin(\theta_2-\theta_1) = 0$.

This corresponds to the case $\theta_2 = \theta_1 + \pi$ and $\theta_2 = \theta_1 + 2\pi$, that is to the planar configuration and to the knife edge. In those cases, the forced response in general exhibits a logarithmic singularity. The derivation of this singular solution is provided in appendix B.

Nevertheless, a regular forced response can still be obtained for the planar configuration if $V_{n1} = V_{n2}$ and for the knife edge if $V_{n1} = -V_{n2}$. This response is degenerated and given, for both cases, by

$$u_\parallel^- = \frac{-V_{n1} + V}{\sin(\theta_1 - \theta_c)} \; ; \quad u_\parallel^+ = \frac{V}{\sin(\theta_1 + \theta_c)}, \quad \text{if} \quad \theta_1 \neq \theta_c, \tag{3.14}$$

and

$$u_\parallel^- = V \; ; \quad u_\parallel^+ = \frac{V_{n1}}{\sin(2\theta_c)}, \quad \text{if} \quad \theta_1 = \theta_c. \tag{3.15}$$

In both equations, V is an undetermined constant which is associated with an uniform flow parallel to the boundary.

3.3. *Inviscid singular eigenmodes*

The solutions obtained in the previous section satisfy the boundary conditions (3.8) on $\mathcal{P}_1$ and $\mathcal{P}_2$. However, they may not describe the complete solution in the domain D. Any function that satisfies non-penetration conditions on $\mathcal{P}_1$ and $\mathcal{P}_2$, and the condition of radiation could, in principle, be added to the solution. In this section, we demonstrate that many such solutions exist. We refer to them as *eigenmodes*, since they satisfy homogeneous boundary solutions. Of particular interest are the singular eigenmodes, as they may dominate the particular solution obtained in the previous section.

Since the singularities are expected to lie along the characteristics issued from the origin, the singular solutions naturally depend on the number of such characteristics within the fluid domain. This leads to four distinct cases, corresponding to 1, 2, 3 or 4 singular directions. Figure 2 illustrates the case with four singular directions. Other examples with 1, 2, or 3 singular directions will be given below.

We will show that singular solutions of the form $|x_\perp|^\alpha$ can be compatible with both the conditions at infinity and the condition of non-penetration on the two planes $\mathcal{P}_1$ and $\mathcal{P}_2$, for particular values of α. To derive these eigenmodes, it is convenient to work with the streamfunction Ψ and use (3.4). The non-penetration condition on the two planes $\mathcal{P}_1$ and $\mathcal{P}_2$ can then be expressed as

$$\Psi(\mathbf{x} \in \mathcal{P}_1) = 0, \tag{3.16a}$$

$$\Psi(\mathbf{x} \in \mathcal{P}_2) = C, \tag{3.16b}$$

where C is a constant. A streamfunction is defined up to an arbitrary constant. Note that we have chosen this constant to be zero on $\mathcal{P}_1$ [see eq. 3.16(a)]. The constant C then measures the radial flux of the solution between $\mathcal{P}_1$ and $\mathcal{P}_2$:

$$F_r = \int_{\theta_1}^{\theta_2} u_r r d\theta = \Psi(\mathbf{x} \in \mathcal{P}_2) - \Psi(\mathbf{x} \in \mathcal{P}_1) = C \; . \tag{3.17}$$

If we consider an expression of the form $a_-|x_\perp^-|^\alpha + a_+|x_\perp^+|^\alpha$ the coefficients a_- and a_+ are expected to change when crossing the singularity lines $x_\perp^\pm = 0$, that is when we moving from a sector S_j to the next, S_{j+1}. Here we fix θ_1 in the interval $(-\theta_c, \theta_c)$, such that the sectors S_1 and S_2 are separated by the line $x_\perp^- = 0$. As we shall see below, the analysis does not change if θ_1 lies outside this interval.

In the most complex case, there are four singular directions, so we expect five expres-

sions for Ψ, each of the form

$$\Psi = a_-^{(j)}|x_\perp^-|^\alpha + a_+^{(j)}|x_\perp^+|^\alpha \tag{3.18}$$

valid within each sector S_j, for $j = 1, ..., 5$.

If we fix the amplitude such that $a_-^{(1)} = 1$, the solution in S_1 is immediately obtained by applying the boundary condition (3.16a) on $\mathcal{P}_1$ which gives

$$\Psi = |x_\perp^-|^\alpha - |K_1|^\alpha |x_\perp^+|^\alpha \quad \text{for} \quad \mathbf{x} \in S_1 \ . \tag{3.19}$$

To obtain the solution in S_2, we apply the radiation condition for the component propagating in the direction $\mathbf{e}_\parallel^-$, which yields

$$\Psi = |x_\perp^-|^\alpha e^{-\mathrm{i}\pi\alpha} - |K_1|^\alpha |x_\perp^+|^\alpha \quad \text{for} \quad \mathbf{x} \in S_2 \ . \tag{3.20}$$

Similarly, the expressions in the successive sectors S_3, S_4 and S_5, obtained by enforcing the radiation condition in the singular directions crossed, are:

$$\Psi = |x_\perp^-|^\alpha e^{-\mathrm{i}\pi\alpha} - |K_1|^\alpha |x_\perp^+|^\alpha e^{\mathrm{i}\pi\alpha} \quad \text{for} \quad \mathbf{x} \in S_3 \ ; \tag{3.21a}$$

$$\Psi = |x_\perp^-|^\alpha e^{-2\mathrm{i}\pi\alpha} - |K_1|^\alpha |x_\perp^+|^\alpha e^{\mathrm{i}\pi\alpha} \quad \text{for} \quad \mathbf{x} \in S_4 \ , \tag{3.21b}$$

$$\Psi = |x_\perp^-|^\alpha e^{-2\mathrm{i}\pi\alpha} - |K_1|^\alpha |x_\perp^+|^\alpha e^{2\mathrm{i}\pi\alpha} \quad \text{for} \quad \mathbf{x} \in S_5 \ . \tag{3.21c}$$

Using the last expression in S_5, we can apply the boundary condition (3.16b) on $\mathcal{P}_2$:

$$\Psi(x_\perp^- = K_2 x_\perp^+) = C \tag{3.22}$$

which gives, for $\alpha \neq 0$, that $C = 0$ and

$$|K_2|^\alpha e^{-2\mathrm{i}\pi\alpha} - |K_1|^\alpha e^{2\mathrm{i}\pi\alpha} = 0 \ . \tag{3.23}$$

This last equation prescribes the following values of α

$$\alpha = \alpha_n^{(4)} = \frac{2n}{4 - \dfrac{\mathrm{i}}{\pi}\log\left|\dfrac{K_1}{K_2}\right|}, \tag{3.24}$$

where n is a non-zero integer. The index (4) in $\alpha_n^{(4)}$ indicates that this result corresponds to the case of four singular directions, i.e., when $\theta_2 > 2\pi - \theta_c$. When there are fewer singular directions in the domain, one should use the corresponding expression for Ψ to apply the boundary condition on $\mathcal{P}_2$. For instance, if θ_2 lies in S_3, there are two singular directions, and one should use equation (3.21a) for Ψ, which leads to

$$\alpha = \alpha_n^{(2)} = \frac{2n}{2 - \dfrac{\mathrm{i}}{\pi}\log\left|\dfrac{K_1}{K_2}\right|}. \tag{3.25}$$

The general result for p singular directions take a simple form which can be written as

$$\alpha_n^{(p)} = \frac{2n}{p - \dfrac{\mathrm{i}}{\pi}\log\left|\dfrac{K_1}{K_2}\right|}. \tag{3.26}$$

This expression remains valid even when θ_1 does not belong to the interval $(-\theta_c, \theta_c)$. Indeed, if we continue to define the sectors S_j in counterclockwise order starting from $\mathcal{P}_1$, the expressions (3.19) and (3.21a,c) for Ψ in sectors S_1, S_3 and S_5 remain unchanged.

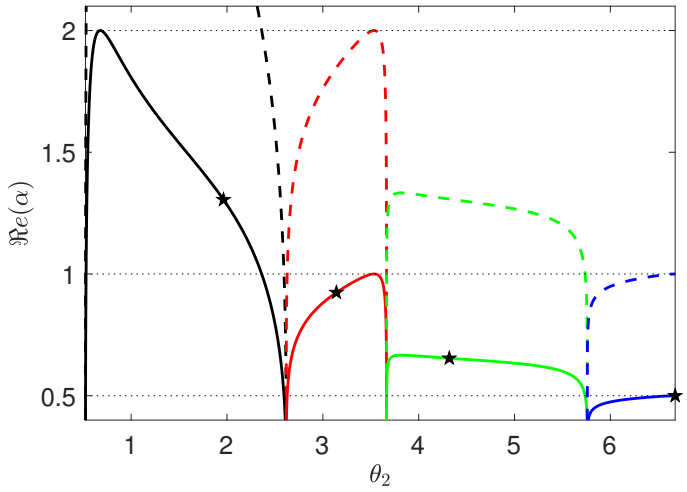

FIGURE 3. Real part of $\alpha_n^{(p)}$ versus θ_2 for $\theta_1 = \pi/8$ and $\theta_c = \pi/6$. Solid lines: $n = 1$, dashed lines: $n = 2$. Line color changes as p changes ($p = 1$: black; $p = 2$: red; $p = 3$: green; $p = 4$: blue. Stars indicated the parameters used for streamline plots in figure 4.

Only the expressions for Ψ in sector S_2 and S_4 are modified, and become

$$\Psi = |x_\perp^-|^\alpha - (-K_1)^\alpha |x_\perp^+|^\alpha e^{\mathrm{i}\pi\alpha} \quad \text{for} \quad \mathbf{x} \in S_2 \ , \tag{3.27a}$$

$$\Psi = |x_\perp^-|^\alpha e^{-\mathrm{i}\pi\alpha} - |K_1|^\alpha |x_\perp^+|^\alpha e^{2\mathrm{i}\pi\alpha} \quad \text{for} \quad \mathbf{x} \in S_4. \tag{3.27b}$$

This occurs when the singular direction crossed between S_1 and S_2 is $x_\perp^+ = 0$ instead of $x_\perp^- = 0$. This modication does not affect the equation satisfied by α. Therefore, we obtain the same eigenvalue (3.26) for the index α.

Similar singular solutions were derived in stratified fluids in the context of the scattering problem (e.g. Wunsch, 1969; Hurley, 1970). They correspond to the complex conjugate of our expressions, owing to the different radiation conditions of internal waves. Wunsch (1969) obtained expression (3.26) for special cases, while Hurley (1970) derived it for all p.

The first notable feature of expression (3.26) is that it generally yields complex values for α. However, there is an important exception: when $|K_1/K_2| = 1$ all the values of α prescribed by (3.26) are real. This occurs in specific situations: when $p = 1$ or $p = 3$, the condition is satisfied when $\tan^2\theta_c \cos\theta_1 \cos\theta_2 = \sin\theta_1 \sin\theta_2$, whereas for $p = 2$, it holds when $\theta_2 = \pi + \theta_1$ (planar case), and for $p = 4$, when $\theta_2 = 2\pi + \theta_1$ (knife-edge case).

Another important property is that the eigenvalues $\alpha_n^{(p)}$ are ordered. As soon as there is at least one singular direction in the domain (i.e. $p \geq 1$), the real part of $\alpha_n^{(p)}$ strictly increases with n, and we have

$$\Re e(\alpha_n^{(p)}) = n\delta^{(p)} \quad \text{with} \quad \delta^{(p)} = \frac{2p}{p^2 + ((1/\pi)\log|K_1/K_2|)^2} > 0. \tag{3.28}$$

The velocity field associated with these solutions has a (singularity) index of $\alpha_n^{(p)} - 1$. It is therefore singular whenever $\Re e(\alpha_n^{(p)}) < 1$. However, a physically relevant solution must have a finite energy; that is, the velocity field should remain square-integrable. This leads to the condition $\Re e(\alpha_n^{(p)}) \geq 1/2$. This, in turn, prescribes a minimum value $n_o^{(p)} > 0$ of the integer n for each value of p.

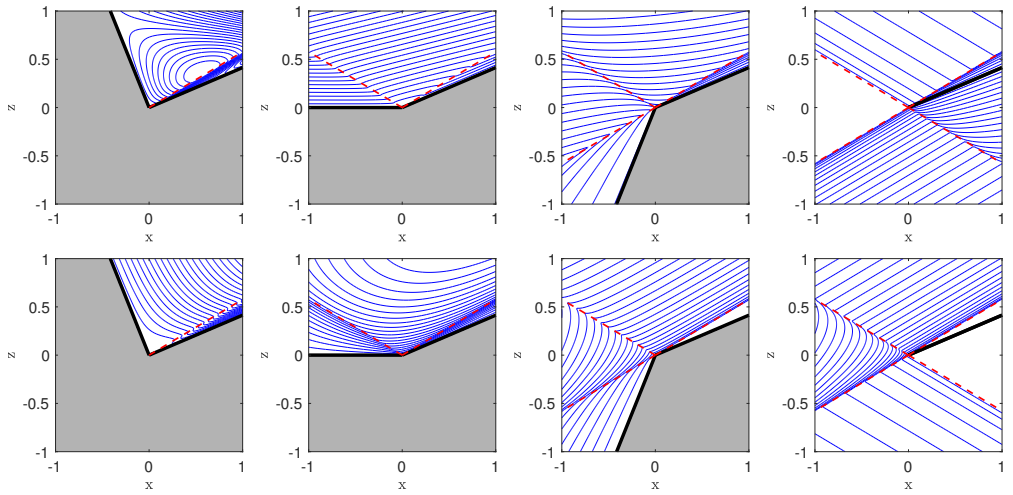

FIGURE 4. Instantaneous streamlines of singular eigenmodes. Contour levels of $\Re e(\Psi)$ (top) and $\Im m(\Psi)$ (bottom) given by (3.19), (3.20) and (3.21a-c) for $\theta_1 = \pi/8$, $\theta_c = \pi/6$. From left to right: $\theta_2 = 5\pi/8$ ($p = 1$, $\alpha = \alpha_1^{(1)} \approx 1.31 - \mathrm{i}0.95$) ; $\theta_2 = \pi$ ($p = 2$, $\alpha = \alpha_1^{(2)} \approx 0.92 - \mathrm{i}0.26$); $\theta_2 = 11\pi/8$ ($p = 3$, $\alpha = \alpha_1^{(3)} \approx 0.65 - \mathrm{i}0.09$); $\theta_2 = 17\pi/8$ ($p = 4$, $\alpha = \alpha_1^{(4)} = 1/2$).

Since $\Re e(\alpha_n^{(p)})$ increases strictly with n, any physically relevant solution of the form $\sum_{n=n_o^{(p)}}^{\infty} A_n \Psi_n$ will, in the limit $|x_\perp^{\pm}| \to 0$ be dominated by its first term. We therefore expect to observe the eigensolution corresponding to $n = n_o^{(p)}$ near the singularities. For $p = 3$ and 4, this eigensolution always has a $\Re e(\alpha_n^{(p)}) < 1$, so its velocity field is singular. The velocity field is also singular for $p = 2$ if $|K_1/K_2| \neq 1$, and for $p = 1$ if $|\log|K_1/K_2|| > \pi$.

In figure 3, we show the variation of $\Re e(\alpha_n^{(p)})$ as a function of θ_2 for $n = 1, 2$ and fixed values of θ_1 and θ_c. We observe singular behavior in these curves near the critical angles where $\log|K_1/K_2|$ diverges. Additionally, for $p = 1$ (i.e. $\alpha_2 < \pi - \alpha_c$), $\Re e(\alpha_1^{(1)})$ exceeds 1 over a large interval of θ_2. This implies that the velocity of the eigenmodes remains continuous for these values. Conversely, for $p = 4$ (i.e. $\alpha_2 > 2\pi - \theta_c$), $\Re e(\alpha_1^{(4)})$ is less than $1/2$, indicating that $n_o^{(4)} \geq 2$, except for $\theta_2 = 2\pi + \theta_1$, for which the $\alpha_1^{(4)} = 1/2$.

The streamlines, defined as the level curves of constant Ψ, are plotted in figure 4 for the parameters indicated by a black star in figure 3. Both the real and imaginary parts of Ψ are shown. These streamline patterns correspond to those observed at two instants separated by a quarter of the oscillation period.

As previously mentioned, the velocity field associated with the eigensolutions exhibits a stronger singularity than Ψ. Its expression can be derived from Ψ using equations (3.5), (3.6) and (3.7). For future reference, we provide below the transverse velocity u_y corresponding to the form of Ψ given in (3.19), (3.20) and (3.21), with a slightly different

normalisation (where the amplitude is divided by α).

$$u_y = \mathrm{i}\left(|x_\perp^-|^{\alpha-1} + |K_1|^\alpha |x_\perp^+|^{\alpha-1}\right) \quad \text{for} \quad \mathbf{x} \in S_1 \tag{3.29a}$$

$$u_y = \mathrm{i}\left(|x_\perp^-|^{\alpha-1} e^{-\mathrm{i}\pi(\alpha-1)} + |K_1|^\alpha |x_\perp^+|^{\alpha-1}\right) \quad \text{for} \quad \mathbf{x} \in S_2 \tag{3.29b}$$

$$u_y = \mathrm{i}\left(|x_\perp^-|^{\alpha-1} e^{-\mathrm{i}\pi(\alpha-1)} + |K_1|^\alpha |x_\perp^+|^{\alpha-1} e^{\mathrm{i}\pi(\alpha-1)}\right) \quad \text{for} \quad \mathbf{x} \in S_3 \tag{3.29c}$$

$$u_y = \mathrm{i}\left(x_\perp^-|^{\alpha-1} e^{-2\mathrm{i}\pi(\alpha-1)} + |K_1|^\alpha |x_\perp^+|^{\alpha-1} e^{\mathrm{i}\pi(\alpha-1)}\right) \quad \text{for} \quad \mathbf{x} \in S_4 \tag{3.29d}$$

$$u_y = \mathrm{i}\left(|x_\perp^-|^{\alpha-1} e^{-2\mathrm{i}\pi(\alpha-1)} + |K_1|^\alpha |x_\perp^+|^{\alpha-1} e^{2\mathrm{i}\pi(\alpha-1)}\right) \quad \text{for} \quad \mathbf{x} \in S_5 \tag{3.29e}$$

This different choice of normalization will be justified below.

In appendix C, we demonstrate how these singular eigenmodes emerge near the wedge apex in two known exact global inviscid solutions.

We conclude this section by highlighting one final important property of the inviscid solutions obtained here. We have seen that they all satisfy $C = 0$ in 3.16(b). This implies that all these solutions exhibit zero radial velocity flux through the wedge:

$$F_r = \int_{\theta_1}^{\theta_2} u_r r d\theta = \Psi(\theta_2) - \Psi(\theta_1) = 0 \ . \tag{3.30}$$

As a result, none of these solutions can therefore be used to balance a possible viscous flux generated in the boundary layer.

To address this limitation, we will introduce a distinct eigensolution corresponding to the degenerate case $n = 0$. This particular eigensolution is derived in the next section.

3.4. *Dirac eigenmode*

The value $n = 0$ in the formula (3.26) gives $\alpha_n^{(p)} = 0$, for which the expressions (3.19), (3.20) and (3.21) yield a constant streamfunction. In that case, the streamfunction singularity must be searched in the form $\log|x_\perp^\pm|$. Using the same approach, we obtain the following expressions for Ψ in each section S_j

$$\Psi = \log|x_\perp^-| - \log|K_1 x_\perp^+| \quad \text{for} \quad \mathbf{x} \in S_1 \tag{3.31a}$$

$$\Psi = \log|x_\perp^-| - \mathrm{i}\pi - \log|K_1 x_\perp^+| \quad \text{for} \quad \mathbf{x} \in S_2 \tag{3.31b}$$

$$\Psi = \log|x_\perp^-| - 2\mathrm{i}\pi - \log|K_1 x_\perp^+| \quad \text{for} \quad \mathbf{x} \in S_3 \tag{3.31c}$$

$$\Psi = \log|x_\perp^-| - 3\mathrm{i}\pi - \log|K_1 x_\perp^+| \quad \text{for} \quad \mathbf{x} \in S_4 \tag{3.31d}$$

$$\Psi = \log|x_\perp^-| - 4\mathrm{i}\pi - \log|K_1 x_\perp^+| \quad \text{for} \quad \mathbf{x} \in S_5 \tag{3.31e}$$

Since $\mathcal{P}_2$ is defined by $x_\perp^- = K_2 x_\perp^+$, the boundary condition (3.16b) on $\mathcal{P}_2$ is automatically satisfied, regardless of the number of singular directions. This solution actually corresponds to a purely radial flow in the (x, z) plane. Using the expression of $x_\perp^\pm$ in terms of the polar coordinates (r, θ) and the equations

$$u_r = \frac{1}{r}\frac{\partial \Psi}{\partial \theta} \quad , \quad u_\theta = -\frac{\partial \Psi}{\partial r} \tag{3.32}$$

we indeed obtain

$$u_r = \frac{\sin(2\theta_c)}{r(\cos^2\theta_c - \cos^2\theta)} \quad , \quad u_\theta = 0 \tag{3.33}$$

and, from (3.3), a simple, unique expression for the transverse velocity

$$u_y = \frac{2\mathrm{i}\sin\theta_c \cos\theta}{r(\cos^2\theta - \cos^2\theta_c)}. \tag{3.34}$$

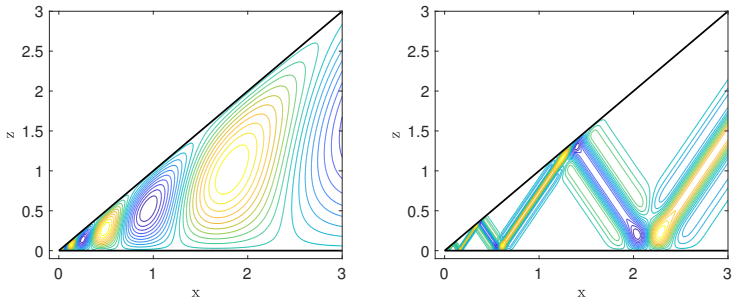

(a) (b)

FIGURE 5. Examples of inviscid solutions obtained in a wedge without singular direction. Contour levels of $\Re e(\Psi)$ obtained from (3.38) for $\theta_1 = 0$, $\theta_2 = \pi/4$, $\theta_c = \pi/3$ for (a): $f(z) = z$, and (b): $f(z) = e^{5z}$.

These expressions do not depend on the number of singular directions and are valid in all sectors S_j.

Unlike the solutions found in the previous section, this solution has a non-zero radial flux, given by

$$F_r^{\text{Dirac}} = \int_{\theta_1}^{\theta_2} u_r r d\theta = \Psi(\theta_2) - \Psi(\theta_1) = -\log\left|\frac{K_1}{K_2}\right| - \mathrm{i}p\pi \tag{3.35}$$

where p is the number of singular directions present in the domain.

It is worth mentioning that the velocity of the Dirac eigenmode is not square-integrable. We thus claim that it cannot be present in any inviscid solution. We shall see below that it can nevertheless be observed when the forcing is of viscous origin.

3.5. *Solutions in a sector without singularity lines*

When neither of the characteristics lines $x_\perp^- = 0$ and $x_\perp^+$ lies within the fluid domain, the singularity generated from the wedge cannot propagate into the fluid: it remains confined to the origin. This situation corresponds to the case where $\mathcal{P}_2$ is within the sector S_1.

The solutions derived in the previous sections remain valid in that case; they correspond to the value $p = 0$. However, since no outer boundary condition is applied, these solutions could, a priori, also describe situations in which waves propagate toward the origin.

Moreover, the solutions of section §3.3 are not ordered anymore, as $\Re e(\alpha_n^{(0)}) = 0$ for all n. More precisely, the nth eigenmode can be written as

$$\Psi_n = (|x_\perp^-|^{\mathrm{i}\alpha_0})^n - (|K_1|^{\mathrm{i}\alpha_0}|x_\perp^+|^{\mathrm{i}\alpha_0})^n \tag{3.36}$$

where α_0 is a real number given by

$$\alpha_0 = \frac{2\pi}{\log\left|\dfrac{K_1}{K_2}\right|}. \tag{3.37}$$

More generally, any expression of the form

$$\Psi = f(|x_\perp^-|^{\mathrm{i}\alpha_0}) - f(|K_1|^{\mathrm{i}\alpha_0}|x_\perp^+|^{\mathrm{i}\alpha_0}) \tag{3.38}$$

satisfies the non-penetration boundary condition on both $\mathcal{P}_1$ and $\mathcal{P}_2$, and is therefore a solution. Streamlines of such solutions are illustrated in figure 5 for the specific choices $f(z) = z$ and $f(z) = e^{5z}$. Note that these solutions can take the form of either vortices

(fig. 5(a)) or concentrated beams (fig. 5(b)), possibly describing the solution observed near one wedge of a librating triangle [see figure 11(a) in section §5.3].

These solutions have no radial flux. If a radial flux is present, one should add the dirac solution which is also valid for $p = 0$ and always exhibits a radial flux.

4. Viscous analysis

The previous section focused on purely inviscid solutions. In this section, we show how a viscous solution can be derived from these results in the limit of small Ekman numbers. This step will be useful for comparison with the DNS results presented in the next section.

4.1. *Viscous smoothing of the inviscid singularities*

A viscous approximation that smooths singularities of the form (3.9) was first introduced by Moore & Saffman (1969) for rotating fluids. A similar solution was also proposed by Thomas & Stevenson (1972) for stratified fluids. This approach has since been used in many studies, to describe the far field from a localized source (e.g., Voisin, 2003), the near field near critical points (Le Dizès & Le Bars, 2017; Le Dizès, 2024) or the propagation of inertial wave beams in spherical shells (He *et al.*, 2022, 2023; Chang *et al.*, 2026).

Moore & Saffman (1969) showed that there exists a similarity solution of the form

$$u_\parallel^+(x_\parallel^+, x_\perp^+, E) \sim \left(\frac{\sin\theta_c}{E|x_\parallel^+|}\right)^{\mu/3} h_\mu(\eta^+) \quad , \tag{4.1}$$

with

$$\eta^+ = x_\perp^+ \left(\frac{\sin\theta_c}{E|x_\parallel^+|}\right)^{1/3} \quad . \tag{4.2}$$

such that

$$\begin{aligned} u_\parallel^+ &\sim \frac{1}{|x_\perp^+|^\mu} \qquad \text{as} \quad \eta^+ \to +\infty, \\ u_\parallel^+ &\sim \frac{e^{-\mathrm{i}\pi\mu}}{|x_\perp^+|^\mu} \qquad \text{as} \quad \eta^+ \to -\infty. \end{aligned} \tag{4.3}$$

The function $h_\mu(\eta)$ is defined by

$$h_\mu(\eta) = \frac{e^{-\mathrm{i}\mu\pi/2}}{\Gamma(\mu)} \int_0^{+\infty} e^{-p^3} e^{\mathrm{i}p\eta} p^{\mu-1} dp \tag{4.4}$$

where $\Gamma(\mu)$ is the Gamma function (Abramowitz & Stegun, 1965, p. 255). The above expression for h_μ is, in principle, defined only if $\Re e(\mu) > 0$. If $\Re e(\mu) \leq 0$, one must interpret the integral in the sense of Hadamard's finite part, as discussed in detail by Voisin (2003). Alternatively, when $\mu \neq -n$ (with n a positive integer), the function h_μ can be defined recursively using the relation (Voisin, 2003):

$$h_\mu(\eta) = -3\mathrm{i}(\mu+2)(\mu+1)h_{\mu+3}(\eta) + \eta h_{\mu+1}(\eta) \ . \tag{4.5}$$

Expression (4.1) describes the velocity field propagating in the direction $x_\parallel^+ > 0$. It provides a viscous regularization of the inviscid singularity present between sectors S_2 and S_3 in the configuration shown in figure 2(b). This expression could, in principle, be extended into S_1 as there is no singularity for this wave between S_1 and S_2. However, as it describes a wave propagating in the direction $x_\parallel^+ > 0$, it cannot cross the line $x_\parallel^+ = 0$.

This solution is therefore valid only in the sectors T_2 and T_3, as shown in figure 2(b). The velocity field propagating in the direction of $-\mathbf{e}_\parallel^+$ is expected to have a similar expression but with η replaced by $-\eta$ to satisfy the adequate radiation condition. The transition from one expression to the other occurs along the line $x_\parallel^+ = 0$. However, the proper phase factor depends on the sign of $x_\perp^+$ along this line. Specifically, for the wave propagating in the direction of $-\mathbf{e}_\parallel^+$, one should use :

$$u_\parallel^+(x_\parallel^+, x_\perp^+, E) \sim e^{\mathrm{i}\mu\pi} \left(\frac{\sin\theta_c}{E|x_\parallel^+|} \right)^{\mu/3} h_\mu(-\eta^+) \quad , \quad \text{if} \quad x_\perp^+ > 0 \tag{4.6a}$$

$$u_\parallel^+(x_\parallel^+, x_\perp^+, E) \sim e^{-\mathrm{i}\mu\pi} \left(\frac{\sin\theta_c}{E|x_\parallel^+|} \right)^{\mu/3} h_\mu(-\eta^+) \quad , \quad \text{if} \quad x_\perp^+ < 0 \ . \tag{4.6b}$$

This implies that, in the configuration shown in 2(b), expression (4.6a) describes the solution in sector T_1, while expression (4.6b) applies in sectors T_4 and T_5.

The same procedure can be done for the wave propagating in the direction $\mathbf{e}_\parallel^-$ whose inviscid approximation satisfies

$$u_\parallel^- \sim \frac{1}{|x_\perp^-|^\mu} \ , \quad \text{for} \quad \mathbf{x} \in S_1 \quad , \qquad u_\parallel^- \sim \frac{e^{\mathrm{i}\pi\mu}}{|x_\perp^-|^\mu} \ , \quad \text{for} \quad \mathbf{x} \in S_2. \tag{4.7}$$

It leads to

$$u_\parallel^-(x_\parallel^-, x_\perp^-, E) \sim \left(\frac{\sin\theta_c}{E|x_\parallel^-|} \right)^{\mu/3} h_\mu(\eta^-) \quad , \quad \text{for} \quad \mathbf{x} \in T_1 \ \& \ T_2 \tag{4.8a}$$

$$u_\parallel^-(x_\parallel^-, x_\perp^-, E) \sim e^{\mathrm{i}\mu\pi} \left(\frac{\sin\theta_c}{E|x_\parallel^-|} \right)^{\mu/3} h_\mu(-\eta^-) \quad , \quad \text{for} \quad \mathbf{x} \in T_3 \ \& \ T_4 \tag{4.8b}$$

$$u_\parallel^-(x_\parallel^-, x_\perp^-, E) \sim e^{2\mathrm{i}\mu\pi} \left(\frac{\sin\theta_c}{E|x_\parallel^-|} \right)^{\mu/3} h_\mu(\eta^-) \quad , \quad \text{for} \quad \mathbf{x} \in T_5 \tag{4.8c}$$

with

$$\eta^- = x_\perp^- \left(\frac{\sin\theta_c}{E|x_\parallel^-|} \right)^{1/3} \ . \tag{4.9}$$

A complete viscous approximation for the transverse velocity whose inviscid expression

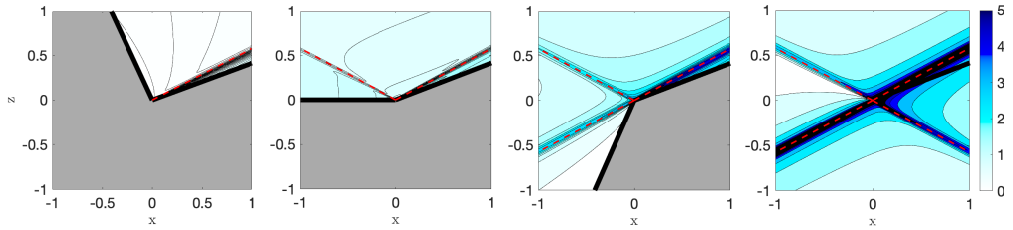

FIGURE 6. Transverse velocity amplitude $|u_y|$ of singular eigenmodes for $\theta_1 = \pi/8$, $\theta_c = \pi/6$ and $E = 10^{-6}$ for the configurations illustrated in figure 4. Thick black lines: boundaries. Red dashed lines: singular directions. The colormap is the same on all plots. From left to right: $\theta_2 = 5\pi/8$; $\theta_2 = \pi$; $\theta_2 = 11\pi/8$; $\theta_2 = 17\pi/8$.

is given by (3.29) can then obtained as:

$$u_y \sim \mathrm{i}K_\alpha \left(e^{-\mathrm{i}\pi(\alpha-1)} |x_\parallel^-|^{\frac{\alpha-1}{3}} h_{1-\alpha}(\eta^-) + e^{-\mathrm{i}\pi(\alpha-1)} |K_1|^\alpha |x_\parallel^+|^{\frac{\alpha-1}{3}} h_{1-\alpha}(-\eta^+) \right) \quad \text{for} \quad \mathbf{x} \in T_1, \tag{4.10a}$$

$$u_y \sim \mathrm{i}K_\alpha \left(e^{-\mathrm{i}\pi(\alpha-1)} |x_\parallel^-|^{\frac{\alpha-1}{3}} h_{1-\alpha}(\eta^-) + |K_1|^\alpha |x_\parallel^+|^{\frac{\alpha-1}{3}} h_{1-\alpha}(\eta^+) \right) \quad \text{for} \quad \mathbf{x} \in T_2, \tag{4.10b}$$

$$u_y \sim \mathrm{i}K_\alpha \left(e^{-2\mathrm{i}\pi(\alpha-1)} |x_\parallel^-|^{\frac{\alpha-1}{3}} h_{1-\alpha}(-\eta^-) + |K_1|^\alpha |x_\parallel^+|^{\frac{\alpha-1}{3}} h_{1-\alpha}(\eta^+) \right) \quad \text{for} \quad \mathbf{x} \in T_3, \tag{4.10c}$$

$$u_y \sim \mathrm{i}K_\alpha \left(e^{-2\mathrm{i}\pi(\alpha-1)} |x_\parallel^-|^{\frac{\alpha-1}{3}} h_{1-\alpha}(-\eta^-) + e^{\mathrm{i}\pi(\alpha-1)} |K_1|^\alpha |x_\parallel^+|^{\frac{\alpha-1}{3}} h_{1-\alpha}(-\eta^+) \right) \quad \text{for} \quad \mathbf{x} \in T_4, \tag{4.10d}$$

$$u_y \sim \mathrm{i}K_\alpha \left(e^{-3\mathrm{i}\pi(\alpha-1)} |x_\parallel^-|^{\frac{\alpha-1}{3}} h_{1-\alpha}(\eta^-) + e^{\mathrm{i}\pi(\alpha-1)} |K_1|^\alpha |x_\parallel^+|^{\frac{\alpha-1}{3}} h_{1-\alpha}(-\eta^+) \right) \quad \text{for} \quad \mathbf{x} \in T_5, \tag{4.10e}$$

with

$$K_\alpha = \left(\frac{\sin\theta_c}{E} \right)^{\frac{1-\alpha}{3}} \quad , \quad \eta^\pm = x_\perp^\pm \left(\frac{\sin\theta_c}{E|x_\parallel^\pm|} \right)^{1/3} . \tag{4.11}$$

These expressions are plotted in figure 6 for $E = 10^{-6}$, using the same configurations as those considered in figure 4. The same colormap is applied to the four cases, demonstrating the increasing velocity amplitude from left to right. This trends is in agreement with the decreasing behavior of the singularity index α.

For the Dirac eigenmode, the viscous approximation can be derived either from (3.34) or directly by taking the limit $\alpha \to 0$ in (4.10a-e). This yields:

$$u_y \sim \mathrm{i}K_0 \left(-|x_\parallel^-|^{-\frac{1}{3}} h_1(\eta^-) - |x_\parallel^+|^{-\frac{1}{3}} h_1(-\eta^+) \right) \quad \text{for} \quad \mathbf{x} \in T_1, \tag{4.12a}$$

$$u_y \sim \mathrm{i}K_0 \left(-|x_\parallel^-|^{-\frac{1}{3}} h_1(\eta^-) + |x_\parallel^+|^{-\frac{1}{3}} h_1(\eta^+) \right) \quad \text{for} \quad \mathbf{x} \in T_2, \tag{4.12b}$$

$$u_y \sim \mathrm{i}K_0 \left(|x_\parallel^-|^{-\frac{1}{3}} h_1(-\eta^-) + |x_\parallel^+|^{-\frac{1}{3}} h_1(\eta^+) \right) \quad \text{for} \quad \mathbf{x} \in T_3, \tag{4.12c}$$

$$u_y \sim \mathrm{i}K_0 \left(|x_\parallel^-|^{-\frac{1}{3}} h_1(-\eta^-) - |x_\parallel^+|^{-\frac{1}{3}} h_1(-\eta^+) \right) \quad \text{for} \quad \mathbf{x} \in T_4, \tag{4.12d}$$

$$u_y \sim \mathrm{i}K_0 \left(-|x_\parallel^-|^{-\frac{1}{3}} h_1(\eta^-) - |x_\parallel^+|^{-\frac{1}{3}} h_1(-\eta^+) \right) \quad \text{for} \quad \mathbf{x} \in T_5. \tag{4.12e}$$

Both expressions (4.10a-e) and (4.12a-e) are viscous approximations of eigensolutions valid near the wedge. They are expected to hold when $|x_\perp^\pm| \ll 1$. These expressions have been normalized to match the inviscid behaviors (3.29a-e) and (3.34), respectively. Each is expected to be multiplied by a (so far unknown) complex amplitude A. As a result, the transverse velocity is expected to scale as $AE^{(\alpha-1)/3}$ and $AE^{-1/3}$ for the zero-radial-flux eigenmode and the Dirac eigenmode, respectively.

For an inviscid forcing, i.e. when $V_{n1}V_{n2} \neq 0$, the amplitude A is independent of E. For the solution (4.10a-e), this leads to a maximum transverse velocity scaling as $E^{(\alpha-1)/3}$. This amplitude becomes large whenever $\Re e(\alpha) < 1$, which corresponds to the condition of existence of a singularity in (3.29a-e). The other condition $\Re e(\alpha) \geq 1/2$, mentioned above, is also obtained from the requirement that the kinetic energy around a singular direction remains finite as $E \to 0$.

In contrast, for a viscous forcing, the amplitude A is, in principle, a function of E. allowing for more singular eigensolutions to be excited. In the next section, we explain in particular how the Dirac solution is excited.

4.2. *Viscous forcing*

When $V_{n1} = V_{n2} = 0$ in (3.8), there is no inviscid forcing. No invisvid response is thus expected. However, as soon as $E > 0$, a viscous response emerges. The tangential and transverse velocity components V_t and V_y of the forcing generate a flow within a boundary layer. This flow is derived in appendix A. A key characteristic of this flow is that it remains confined within a viscous boundary layer of thickness $\sqrt{E}$. Moreover, since V_{t1}, V_{t2}, V_{y1} and V_{y2} are constants, there is no forcing of a normal flow at the order $E^{1/2}$; in other words, there is no Ekman pumping. Yet, as we will see in section §5 a viscous response is observed in the bulk even in that case. We claim that this response corresponds to an inviscid eigenmode. Furthermore, we will show that both the amplitude and the index α can generally be predicted. We have previously identified two types of singular eigenmodes, those in $|x_\perp^\pm|^{\alpha_n^{(p)}}$ with zero radial flux, and the Dirac eigenmode with a non-zero radial flux. We argue that the Dirac eigenmode is excited in order to balance the radial flux generated within the viscous boundary layers.

In the appendix A, we show that a forcing of the form $V_{t1}\mathbf{e}_{t1} + V_{y1}\mathbf{e}_y$ on $\mathcal{P}_1$ induces a viscous boundary layer flow with a tangential flux

$$F_{t1} = \sqrt{E}\left(\frac{V_{t1} - \mathrm{i}V_{y1}}{\lambda_1^+} + \frac{V_{t1} + \mathrm{i}V_{y1}}{\lambda_1^-}\right). \tag{4.13}$$

A similar flow near $\mathcal{P}_2$ produces a tangential flux

$$F_{t2} = \sqrt{E}\left(\frac{V_{t2} + \mathrm{i}V_{y2}}{\lambda_2^+} + \frac{V_{t2} - \mathrm{i}V_{y2}}{\lambda_2^-}\right). \tag{4.14}$$

The boundary layer wavenumbers $\lambda_j^\pm$, $j = 1, 2$ are given by

$$\lambda_j^\pm = \begin{cases} e^{-\mathrm{i}\pi/4}\sqrt{\cos\theta_c \pm \cos\theta_j} & \text{if} \quad \cos\theta_c \pm \cos\theta_j > 0, \\ e^{\mathrm{i}\pi/4}\sqrt{|\cos\alpha_c \pm cos\theta_j|} & \text{if} \quad \cos\theta_c \pm \cos\theta_j < 0. \end{cases} \tag{4.15}$$

The definition of $\mathbf{e}_{t1}$ and $\mathbf{e}_{t2}$ given in figure 1(b), is such that the flux on $\mathcal{P}_1$ is outward, while that on $\mathcal{P}_2$ is inward. The total outward radial flux within the boundary layers is therefore

$$F_r^{BL} = F_{t1} - F_{t2}. \tag{4.16}$$

We argue that this radial flux must be balanced in the bulk by an eigenmode which possesses a non-zero radial flux. Since only the Dirac eigenmode has such a property, it

is the only viable candidate. Its amplitude is then determined by the condition that the sum of both radial fluxes cancels, leading to

$$A = -\frac{F_r^{BL}}{F_r^{\mathrm{Dirac}}}, \tag{4.17}$$

where F_r^{Dirac} is defined in (3.35). This completely prescribes the leading order solution near the apex of the wedge: its transverse velocity amplitude is then Au_y with u_y given by (4.12a-e).

4.3. *Viscous corrections*

The eigensolutions calculated in the previous sections satisfy the non-penetration condition on $\mathcal{P}_1$ and $\mathcal{P}_2$ but they exhibit a strong tangential and transverse velocity on these planes. In a viscous fluid, these velocity components should also vanish on the boundary. This means that a viscous flow is present in the boundary layer in order to cancel these components. Such a flow has been calculated in appendix A for any forcing velocity. Because this flow depends on the tangential coordinate, it induces a Ekman pumping which forces a response in the bulk. This response corresponds to the viscous correction that we want to calculate.

As before, we assume that the planes $\mathcal{P}_1$ and $\mathcal{P}_2$ are not aligned with a singular direction. This allows us to use the inviscid expressions for the eigensolutions. For both the zero-flux solution and the dirac solution, we obtain, on $\mathcal{P}_1$ (with $x_{t_1} > 0$):

$$u_{y_1} = -\frac{2\mathrm{i}\sin\theta_c\cos\theta_1}{\cos^2\theta_c - \cos^2\theta_1}|\sin(\theta_1-\theta_c)|^\alpha x_{t_1}^{\alpha-1}, \quad u_{t_1} = \mathrm{i}\frac{\cos\theta_c}{\cos\theta_1}u_{y_1}, \tag{4.18}$$

and, on $\mathcal{P}_2$ (with $x_{t_2} < 0$):

$$u_{y_2} = \frac{2\mathrm{i}\sin\theta_c\cos\theta_2}{\cos^2\theta_c - \cos^2\theta_2}|\sin(\theta_2-\theta_c)|^\alpha e^{-\mathrm{i}\pi q\alpha}(-x_{t_2})^{\alpha-1}, \quad u_{t_2} = \mathrm{i}\frac{\cos\theta_c}{\cos\theta_2}u_{y_2}, \tag{4.19}$$

where $\alpha = \alpha_n^{(p)}$ for the zero-flux eigenmode and $\alpha = 0$ for the Dirac eigenmode. In equation (4.19), the integer $q = 0, 1, 2$ corresponds to the number of the singular direction $x_\perp^- = 0$ in the fluid domain. This number is different from p which is the number of singular directions (i.e. both $x_\perp^- = 0$ and $x_\perp^+ = 0$) in the fluid domain. The boundary layer flow that is created on each boundary to cancel these velocities generate an Ekman pumping that can be calculated using (A 17). We obtain

$$u_{n1}^{\mathrm{Ekman}} = \sqrt{E}|x_{t_1}|^{\alpha-2}A_1 \quad , \quad u_{n2}^{\mathrm{Ekman}} = \sqrt{E}|x_{t_2}|^{\alpha-2}A_2, \tag{4.20}$$

where A_1 and A_2 are given by

$$A_1 = -\mathrm{i}(1-\alpha)\sin\theta_c|\sin(\theta_1-\theta_c)|^\alpha\left(\frac{1}{(\lambda_1^+)^3}+\frac{1}{(\lambda_1^-)^3}\right), \tag{4.21a}$$

$$A_2 = -\mathrm{i}(1-\alpha)\sin\theta_c|\sin(\theta_2-\theta_c)|^\alpha e^{-\mathrm{i}\pi q\alpha}\left(\frac{1}{(\lambda_2^+)^3}+\frac{1}{(\lambda_2^-)^3}\right). \tag{4.21b}$$

In return, this Ekman pumping yields a response in the bulk that must satisfy (3.8) where V_{n1} and V_{n2} are now the functions u_{n1}^{Ekman} and u_{n2}^{Ekman}. Naturally, a solution with the same behavior in $|x_\perp^\pm|^{\alpha-2}$ can be searched for $u_\parallel^\pm$. If we assume

$$u_\parallel^- = A^-|x_\perp^-|^{\alpha-2}, \quad u_\parallel^+ = A^+|x_\perp^+|^{\alpha-2} \quad \text{for} \quad \mathbf{x}\in S_1, \tag{4.22}$$

we immediately obtain in the other sectors, using the radiation condition,

$$u_\parallel^- = A^-|x_\perp^-|^{\alpha-2}e^{-\mathrm{i}\pi\alpha}, \quad u_\parallel^+ = A^+|x_\perp^+|^{\alpha-2} \quad \text{for} \quad \mathbf{x}\in S_2, \tag{4.23a}$$

$$u_\parallel^- = A^-|x_\perp^-|^{\alpha-2}e^{-\mathrm{i}\pi\alpha}, \quad u_\parallel^+ = A^+|x_\perp^+|^{\alpha-2}e^{\mathrm{i}\pi\alpha} \quad \text{for} \quad \mathbf{x}\in S_3, \tag{4.23b}$$

$$u_\parallel^- = A^-|x_\perp^-|^{\alpha-2}e^{-2\mathrm{i}\pi\alpha}, \quad u_\parallel^+ = A^+|x_\perp^+|^{\alpha-2}e^{\mathrm{i}\pi\alpha} \quad \text{for} \quad \mathbf{x}\in S_4, \tag{4.23c}$$

$$u_\parallel^- = A^-|x_\perp^-|^{\alpha-2}e^{-2\mathrm{i}\pi\alpha}, \quad u_\parallel^+ = A^+|x_\perp^+|^{\alpha-2}e^{2\mathrm{i}\pi\alpha} \quad \text{for} \quad \mathbf{x}\in S_5. \tag{4.23d}$$

The boundary conditions on $\mathcal{P}_1$ and $\mathcal{P}_2$ lead to an inhomogeneous system of two equations for A^- and A^+. As before, one must take the expressions of $u_\parallel^\pm$ in the sector where $\mathcal{P}_2$ belongs. For instance, if $\mathcal{P}_2 \in S_5$ (that is $p=4$ and $q=2$), we obtain

$$-\sin(\theta_1-\theta_c)A^-|K_1|^{\alpha-2} + \sin(\theta_1+\theta_c)A^+ = \frac{A_1\sqrt{E}}{|\sin(\theta_c+\theta_1)|^{\alpha-2}}\ , \tag{4.24a}$$

$$\sin(\theta_2-\theta_c)A^-|K_2|^{\alpha-2}e^{-2\mathrm{i}\pi\alpha} - \sin(\theta_2+\theta_c)A^+e^{+2\mathrm{i}\pi\alpha} = \frac{A_2\sqrt{E}}{|\sin(\theta_c+\theta_2)|^{\alpha-2}}\ . \tag{4.24b}$$

The solution of this system is

$$A^- = \frac{K_1K_2\sqrt{E}}{K_1-K_2}\left(A_1\frac{\sin(\theta_1+\theta_c)}{|\sin(\theta_1-\theta_c)|^\alpha} + A_2\frac{\sin(\theta_2+\theta_c)}{|\sin(\theta_2-\theta_c)|^\alpha}e^{2\mathrm{i}\pi\alpha}\right), \tag{4.25a}$$

$$A^+ = \frac{\sqrt{E}}{K_1-K_2}\left(A_1\frac{\sin(\theta_1-\theta_c)}{|\sin(\theta_1+\theta_c)|^\alpha} + A_2\frac{\sin(\theta_2-\theta_c)}{|\sin(\theta_2+\theta_c)|^\alpha}e^{-2\mathrm{i}\pi\alpha}\right), \tag{4.25b}$$

which becomes, using (4.21) and (3.23):

$$A^- = -\mathrm{i}\sqrt{E}\frac{(1-\alpha)\sin\theta_c K_1K_2\left(\sin(\theta_1+\theta_c)((\lambda_1^+)^{-3}+(\lambda_1^-)^{-3})+\sin(\theta_2+\theta_c)((\lambda_2^+)^{-3}+(\lambda_2^-)^{-3})\right)}{K_1-K_2},$$

$$A^+ = -\mathrm{i}\sqrt{E}\frac{(1-\alpha)\sin\theta_c |K_1|^\alpha\left(\sin(\theta_1-\theta_c)((\lambda_1^+)^{-3}+(\lambda_1^-)^{-3})+\sin(\theta_2-\theta_c)((\lambda_2^+)^{-3}+(\lambda_2^-)^{-3})\right)}{K_1-K_2}.$$

The parameters p and q do not appear in these final expressions. The dependence on the number of singular directions therefore enters only through the singularity index α. From the expressions of $u_\parallel^\pm$ obtained with these values of $A^\pm$, we can also derive, using (3.7), an expression for the transverse velocity u_y.

Starting from these singular inviscid expressions, we can then obtain smoothed viscous expressions by applying the procedure described above. The viscous correction involves the similarity solution h_μ with an index $\mu = 2-\alpha$. This index is increased by 1 compared to the initial solution, corresponding to a viscous beam with a relative amplitude larger by a factor $E^{-1/3}$. Consequently, the amplitude of the viscous correction is then $E^{1/2}E^{-1/3} = E^{1/6}$ smaller than that of the initial solution.

5. Numerical results

In this section, we use several numerical examples to demonstrate that the eigensolutions derived in the previous section are indeed observed in the vicinity of the wedge. We consider two geometries: a square obstacle and a triangular cavity, illustrated in figure 7.

5.1. *Methods*

In all cases, we consider the two-dimensional linearized dynamics of an incompressible fluid in a rotating frame, governed by equations (2.1). Using the characteristic size L of the object as a reference length scale and the inverse of the Coriolis parameter f as a

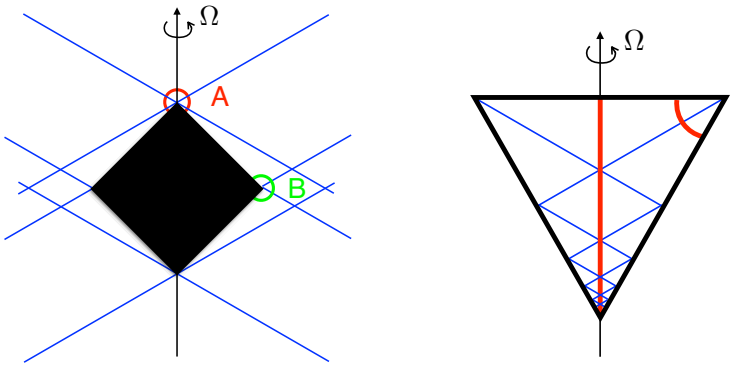

(a) (b)

FIGURE 7. Sketch of the simulated domains. The blue lines represent the singularity lines emitted from the corners for $\omega = \cos(\pi/6)$. The numerical and theoretical profiles are compared along the red and green solid lines. (a) Fluid around a square; (b) Fluid within a triangle.

reference time scale, the dimensionless governing equations are

$$\frac{\partial \boldsymbol{u}}{\partial t} + 2\boldsymbol{e}_z \times \boldsymbol{u} = -\nabla P + E\nabla^2 \boldsymbol{u} - \frac{\chi \boldsymbol{u}}{\tau}, \tag{5.1}$$

$$\nabla \cdot \boldsymbol{u} = 0 \ , \tag{5.2}$$

where E is the Ekman number defined by equation (2.6). The last term in the momentum equation is a linear damping term which absorbs outgoing waves and prevent reflections on the outer boundary of the domain. χ is a stationary mask function which determines where this damping is effective (typically far from the wedge of interest) while τ is a characteristic damping time tuned to minimize wave reflections, and we typically take it equal to the wave period $2\pi/\omega$.

The fluid is forced by imposing various types of boundary conditions on the solid surface. We consider the cases of an inviscid forcing associated with vertical oscillations of the form $u_z(\mathbf{x} \in \mathbf{x}_S) = \sin(\omega t)$, where $\mathbf{x}_S$ is the solid boundary and ω is the forcing frequency. Alternatively, we also consider a purely viscous forcing corresponding to transverse oscillations of the form $u_y(\mathbf{x} \in \mathbf{x}_S) = \sin(\omega t)$. In all cases, the forcing frequency is chosen such that $\theta_c = \pi/6$ while we arbitrarily fix the forcing amplitude to unity.

Following Le Dizès & Favier (2026), we use the spectral-element solver Nek5000 (Fischer, 1997; Deville *et al.*, 2002) to solve the governing equations. The fluid domain is discretised using quadrilateral elements that are refined near the solid boundary to ensure adequate resolution of the viscous boundary layers. The square obstacle is embedded within a larger square cavity whose side length is ten times that of the obstacle. In combination with the linear damping term, this configuration ensures that wave reflections remain negligible. Only the interior of the triangular cavity is discretised and no linear damping is necessary in that confined case. The number of elements depends on the geometry considered: $\mathcal{E} = 2432$ for the square obstacle and $\mathcal{E} = 3267$ for the triangular cavity. The velocity field is discretised within each element using Lagrange polynomial interpolants of order 24. Since the simulations are linear, dealiasing is not required. A third-order time integration is used, where viscous terms are solved implicitely while the Coriolis term is solved explicitely. Equations (5.1) are solved as an initial-value prob-

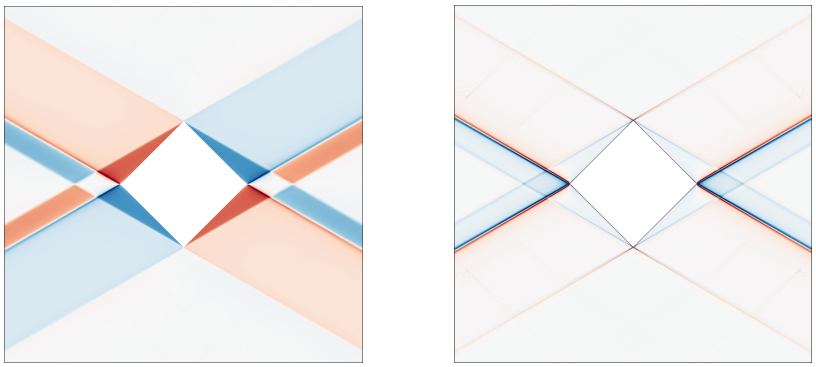

(a) (b)

FIGURE 8. Instantenous snapshots of the transverse velocity from the numerical simulations during the harmonic quasi-stationnary stage. The Ekman number is $E = 10^{-7}$ and the forcing frequency is $\omega = \sin(\pi/6)$ is both cases. (a) Vertical oscillations (inviscid forcing); (b) Transverse oscillations (viscous forcing). The amplitude of the response is much larger in the first case than in the second case.

lem starting from a fluid initially at rest. The simulation is advanced in time until a quasi-stationary harmonic state oscillating at the forcing frequency ω is reached.

5.2. *Results for the square obstacle*

We first consider the simple square geometry illustrated in figure 7(a) and two different forcings: an inviscid forcing corresponding to vertical oscillations of the form $u_z(\mathbf{x} \in \mathbf{x}_S) = \sin(\omega t)$, and a purely viscous forcing corresponding to transverse oscillations of the form $u_y(\mathbf{x} \in \mathbf{x}_S) = \sin(\omega t)$. Snapshots of the harmonic transverse velocity field are shown in figure 8 for the two cases. Movies of the time evolution during one period are available online as supplementary materials.

For the comparison, we focus on two wedges:

- The right wedge (R), which has two singular directions ($p = 2$), with $\theta_1 = -3\pi/4$ and $\theta_2 = 3\pi/4$;
- The top wedge (T), which has four singular directions ($p = 4$) with $\theta_1 = -\pi/4$ and $\theta_2 = 5\pi/4$.

For the inviscid forcing, we expect the solution near each wedge to be well-approximated by a singular eigenmode of the form (4.10) where the index $\alpha_n^{(p)}$ is the smallest index greater than $1/2$.

For the right wedge, $|K_1/K_2| = 7 - 4\sqrt{3}$, the smallest index larger than $1/2$ is then

$$\alpha^{(R)} = \alpha_1^{(2)} = \frac{1}{1 + \frac{\mathrm{i}}{\pi}\log(2+\sqrt{3})} \approx 0.8505 - \mathrm{i}\,0.3565. \tag{5.3}$$

For the left wedge $|K_1/K_2| = 7 + 4\sqrt{3}$, the smallest index larger than $1/2$ is

$$\alpha^{(L)} = \alpha_2^{(4)} = \frac{2}{2 + \frac{\mathrm{i}}{\pi}\log(2-\sqrt{3})} \approx 0.9579 + \mathrm{i}\,0.2008. \tag{5.4}$$

In figure 9, the numerical solution is compared for each wedge with the corresponding singular eigenmode. The transverse component u_y is plotted on the arc of circle of radius $r_0 = 0.1$ for θ between θ_1 and θ_2 for two different times t_0 and $t_1 = t_0 + \pi/(2\omega)$ separated by a quarter of period. For both times, the numerical signal is normalized by the maximum value $\max_\theta |u_\theta|$ for $t = t_0$. The theoretical curves correspond to the approximations obtained from equations (4.10). The amplitude is normalized in the same

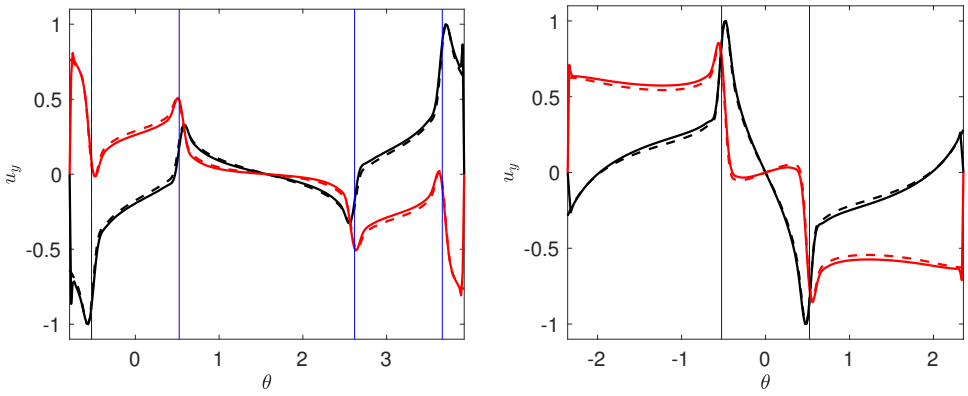

FIGURE 9. Transverse velocity u_y obtained near each wedge on the arc of circle of radius $r_0 = 0.1$ from the wedge, for the inviscid forcing, at two distinct instants t_0 (in black) and $t_1 = t_0 + \pi/(2\omega)$ (in red). Solid lines: numerical results; dashed lines: theoretical results. Thin blue lines indicate the position of the inviscid singularities. Both theoretical and numerical results are normalized by $\max_\theta |u_\theta|$ at $t = t_0$. (a) Top wedge. (b) Right wedge.

way as the numerical data. The only free remaining parameter is the phase (equivalently, the reference time t_0) which is adjusted in order to get the best agreement. These graphs speak for themselves: the agreement is remarkably good for each corner.

For the viscous forcing, top and right wedges have different characteristics in the boundary layer. By symmetry, for the top wedge, the outward flux from one side is equal to inward flux from the other side: the total radial flux in the boundary layer from the top wedge therefore cancels. This is not the case for the right wedge as both outward fluxes are identical from each side. The total outer radial flux in the boundary layer from the right wedge is

$$F_r^{\mathrm{BL}(R)} = 2\sqrt{-1+\sqrt{3}}\sqrt{E}\sin(\omega t + \pi/4) \tag{5.5}$$

for the viscous forcing $u_y(\mathbf{x} \in \mathcal{P}_j) = \sin(\omega t)$ on the boundaries $\mathcal{P}_1$ and $\mathcal{P}_2$.

For the top wedge, we cannot balance an outer flux in the boundary layer by a Dirac eigenmode, as this flux is zero. The solution is therefore expected to be described by a singular eigenmode with zero flux. However, because the forcing is viscous, a more singular solution than for an inviscid forcing is possible. As the amplitude scales as $\sqrt{E}$, the condition of finite energy for a velocity perturbation behaving like $|x_\perp|^{\alpha-1}$ only requires $EE^{2(\Re e(\alpha)-1)/3}E^{1/3} \gg 1$, that is $\Re e(\alpha) > -1$. The smallest $\alpha_n^{(4)}$ satisfying this condition is

$$\alpha_{-2}^{(4)} = -\frac{2}{2 + \frac{\mathrm{i}}{\pi}\log(2-\sqrt{3})} \approx -0.9579 - \mathrm{i}\,0.2008.$$

However, the corresponding eigenmode has a transverse velocity that is antisymmetric with respect to the vertical axis ($\theta = \pi/2$); it is therefore not excited by our symmetric forcing. The one that is excited corresponds to the next index:

$$\alpha_{-1}^{(4)} = -\frac{1}{2 + \frac{\mathrm{i}}{\pi}\log(2-\sqrt{3})} \approx -0.4790 - \mathrm{i}\,0.1004. \tag{5.6}$$

The corresponding eigenmode has the right symmetry. It is this eigenmode that is compared to the numerical solution obtained near the top wedge in figure 10. The comparison is performed with a renormalized amplitude, with the optimal choice of phase, as in the case of the inviscid forcing. Note, however, that the agreement is not as

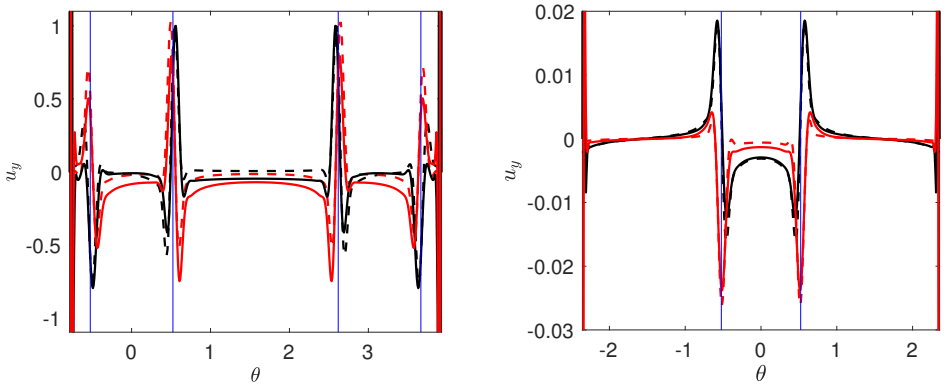

FIGURE 10. Transverse velocity u_y obtained near each corner on an arc of radius $r_0 = 0.1$ from the corner, for the viscous forcing, at two distinct instants t_0 (in black) and $t_1 = t_0 + \pi/(2\omega)$ (in red). Solid lines: numerical results; dashed lines: theoretical results. Thin blue lines indicate the position of the inviscid singularities. (a) Top wedge: comparison with the eigenmode associated with $\alpha = \alpha_{-1}^{(4)}$. Both numerical and theoretical data are normalized by $\max_\theta |u_\theta|$ at $t = t_0$. (b) Right wedge: comparison with the Dirac eigenmode ($\alpha = 0$). The amplitude of the Dirac eigenmode is obtained from (5.8).

good as for the inviscid forcing. We suspect that this is due to the very weak amplitude of the response in that case, which may therefore be influenced by additional corrections.

For the right wedge, the radial flux in the boundary layer must be compensated by an eigensolution that carries a radial flux. If we choose the Dirac solution, this requirement prescribes not only its structure but also its amplitude and phase. For the angles defining the right wedge, the Dirac solution (4.12) with a complex amplitude A exhibit an oscillating radial flux

$$F_r^{\mathrm{Dirac}} = A(-\log(7-4\sqrt{3}) - 2\mathrm{i}\pi)e^{-\mathrm{i}\omega t} + c.c. \tag{5.7}$$

The complex amplitude A must be chosen such that $F_r^{\mathrm{Dirac}} + F_r^{BL} = 0$, which yields

$$A = \frac{\sqrt{-1+\sqrt{3}}}{\log(7-4\sqrt{3}) + 2\mathrm{i}\pi} e^{3\mathrm{i}\pi/4}\sqrt{E} = |\bar{A}|e^{\mathrm{i}\phi_A}\sqrt{E}, \tag{5.8}$$

with

$$|\bar{A}| \approx 0.1255\ , \quad \phi_A \approx 0.3884. \tag{5.9}$$

The agreement observed in figure 10(b), although not perfect, is remarkable for a theory without any adjustable parameter.

5.3. *Results for the triangular cavity*

We now consider the closed geometry illustrated in figure 7(b). This triangular geometry was first studied by Greenspan (1969). Its distinctive feature is that all waves tend to converge toward the bottom wedge, which thus acts as an attractor. We simulated the case of viscous forcing with transverse oscillations $u_y(\mathbf{x} \in \mathbf{x}_S) = \sin(\omega t)$, with $\omega = \cos(\pi/6)$ and $E = 10^{-7}$ as for the previous case. A movie of the transverse velocity field oscillations in the triangle during a period is provided as supplementary material. A snapshot of this movie at a fixed time is displayed in figure 11(a).

The numerical results reveal that the response is dominated by two concentrated beams originating from the two top wedges. These two waves beams converge to the bottom corner after multiple reflections on the inclined boundaries. If nothing is reflected from

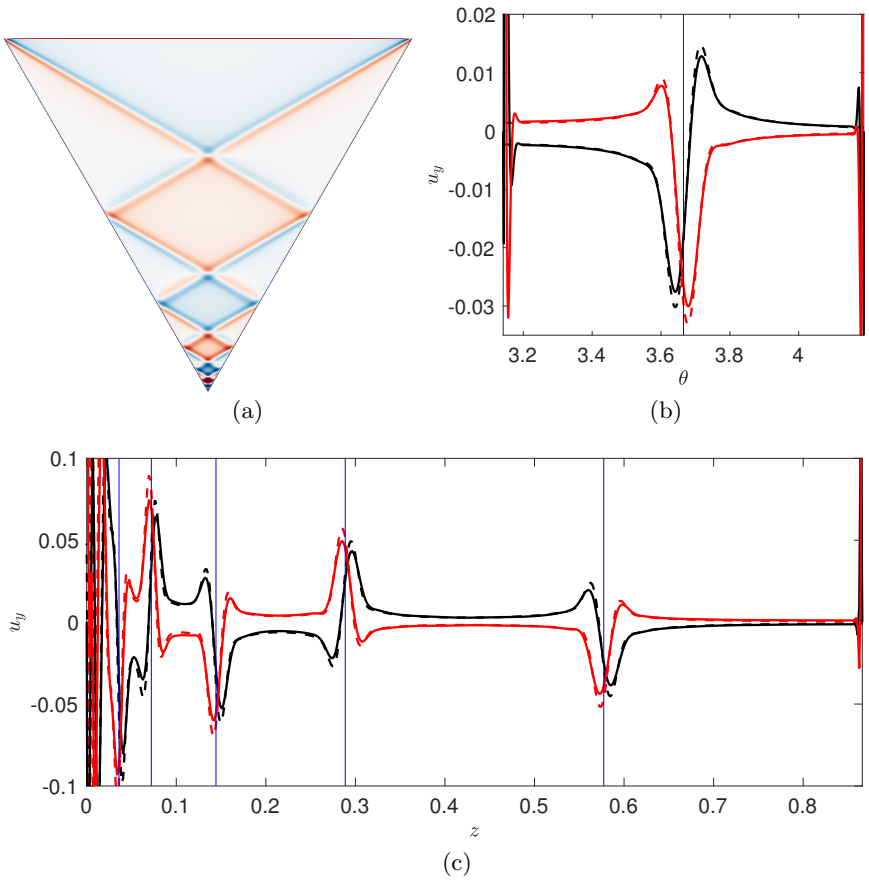

FIGURE 11. (a) Instantenous snapshots of the harmonic transverse velocity in a librating triangle from the numerical simulations. (b-c) Comparison of the transverse velocity u_y at two distinct instants t_0 (in black) and $t_1 = t_0 + \pi/(2\omega)$ (in red). Solid lines: numerical results; dashed lines: theoretical results. Thin blue lines indicate the position of the inviscid singularities. (b) Profile at $r = 0.2$ from the upper right corner. (c) Profile along the vertical line passing through the bottom corner.

this corner, the solution generated close to the top corners could be identical to that of an unbounded domain. In other words, the waves emitted from both top corners would satisfy outward wave boundary conditions. This implies that the present theory also applies to this bounded case.

For a viscous forcing, we have shown that a Dirac singular solution can be generated from the wedge if the tangential flux in the boundary layer does not vanish. This condition holds for both top corners. For the top-right wedge, the tangential flux in the boundary layer generated by libration is:

$$F_r^{\rm BL} = \left(\frac{\sqrt{3} - 1 + \sqrt{\sqrt{3}-1} - \sqrt{\sqrt{3}+1}}{2} + {\rm i}\sqrt{\frac{2+\sqrt{3}}{2}} \right) \sqrt{E}\, e^{-{\rm i}\omega t} + c.c. \qquad (5.10)$$

while the radial flux associated with a Dirac solution of amplitude A from this corner is:

$$F_r^{\rm Dirac} = -A(\log 2 + {\rm i}\pi) e^{-{\rm i}\omega t} + c.c. \qquad (5.11)$$

The cancellation of the total flux $F_r^{\mathrm{BL}} + F_r^{\mathrm{Dirac}}$ yields:

$$A = \left(\frac{\sqrt{3} - 1 + \sqrt{\sqrt{3} - 1} - \sqrt{\sqrt{3} + 1} + \mathrm{i}\sqrt{2}\sqrt{2 + \sqrt{3}}}{2(\log 2 + \mathrm{i}\pi)} \right) \sqrt{E} \approx -(0.220 + \mathrm{i}0.363)\sqrt{E}. \tag{5.12}$$

The numerical solution is compared with the Dirac solution of this amplitude near the top-right corner in figure 11(b). We plot the transverse velocity u_y along the arc-circle located at a distance $r = 0.2$ from the apex of the wedge, at $t = t_0 = 3801.72$ (in black) and $t_1 = t_0 + \pi/(2\omega) \approx 3803.53$ (in red). As shown, the agreement of the numerical results with the theory is excellent.

For the left corner, a Dirac solution of opposite amplitude is generated. If both Dirac solutions emitted for each top corners are propagated within the triangle, and reflected on the boundaries using the reflection rule of a Moore-Saffman solution (as derived in Le Dizès, 2020), a solution can be obtained for the entire domain. This theoretical solution is compared with the numerical solution on the vertical line passing through the bottom corner in figure 11(c). Again, we plot the transverse velocity u_y at the two instants t_0 and t_1. The agreement remains very good, except in the immediate vicinity of the attractor point at the bottom corner. Notably, the theoretical solution is valid not only near the intersection points of the two concentrated beams, but also between these points.

6. Other applications of the results

6.1. *Inviscid scattering problem*

In this section, we examine a related yet distinct problem: the scattering of a plane wave by a wedge. We consider a plane wave incident from infinity onto a wedge and seek to determine the response generated by the topography.

As an illustrative example, consider an incident streamfunction amplitude given by

$$\Psi_I(x_\perp^-) = e^{-\mathrm{i}x_\perp^-}, \tag{6.1}$$

which represents an inviscid plane wave of unit wavenumber propagating in the $-\mathbf{e}_\parallel^-$ direction. The total streamfunction can be written as

$$\Psi(x_\perp^-, x_\perp^+) = \Psi_I(x_\perp^-) + \Psi_R(x_\perp^-, x_\perp^+) \tag{6.2}$$

where Ψ_R is the streamfunction of the scattered field propagating away from the wedge. The total velocity field satisfies non-penetration conditions on the wedge boundaries. Thus the velocity field deduced from Ψ_R satisfies boundary conditions of the form (3.8) on the wedge boundaries, where the normal velocities V_{n1} and V_{n2} are the opposite of the normal velocity of the incident beam on the two planes $\mathcal{P}_1$ and $\mathcal{P}_2$. Close to the origin, these velocities take constant values. The problem of finding the field Ψ_R near the origin and close to the singular directions is therefore identical to the problem treated above. We then anticipate that singular inviscid eigenmodes may be excited by the incident wave.

As an illustration, consider a case with four singular directions (figure 12). According to ray theory (Phillips, 1966), far from the origin, the field Ψ_R should consist of a reflected plane wave propagating in the $\mathbf{e}_\parallel^+$ direction with a constant amplitude in sector S_1, and a transmitted plane wave propagating in the $-\mathbf{e}_\parallel^-$ direction in sector S_5 with an amplitude opposite to that of the incident wave, thereby cancelling the incident field in this sector.

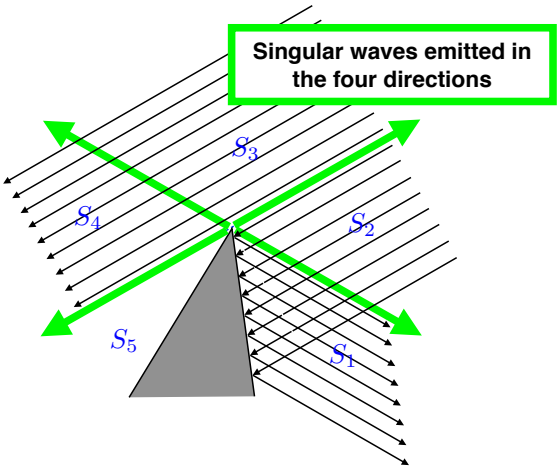

FIGURE 12. Sketch of the scattering problem from a tip with four singular directions. In solid lines are the predictions from ray theory (Phillips, 1966). In green line, the additional singular waves scattered by the tip.

Thus, ray theory predicts that Ψ takes the form

$$\Psi(x_\perp^-, x_\perp^+) = e^{-\mathrm{i}x_\perp^-} - e^{-\mathrm{i}K_1 x_\perp^+} \quad \text{for} \quad \mathbf{x} \in S_1, \tag{6.3a}$$

$$\Psi(x_\perp^-, x_\perp^+) = e^{-\mathrm{i}x_\perp^-} \quad \text{for} \quad \mathbf{x} \in S_2 \cup S_3 \cup S_4, \tag{6.3b}$$

$$\Psi(x_\perp^-, x_\perp^+) = 0 \quad \text{for} \quad \mathbf{x} \in S_5. \tag{6.3c}$$

However, these expressions are not valid near the singular lines because they do not satisfy the condition of radiation. They would imply a jump in Ψ across the singular lines between S_1 and S_2, and between S_4 and S_5, which does not correspond to any admissible singular behavior of a wave propagating outward. We claim instead that a stronger singular field is present in that case, and that this field must be one of the singular inviscid eigenmodes obtained previously. The consequence is that a response should be obtained in the four singular directions. This means that not only is a back-reflected wave produced, but this wave is singular. In the presence of viscosity, this would imply a back-reflected wave with a larger amplitude than that of the incident wave. The amplitude of this wave is $O(E^{(\alpha_n^{(4)}-1)/3})$ where the index $\alpha_n^{(4)}$ of the singular eigenmode is given by (3.24) and satisfies $1/2 \leq \alpha_n^{(4)} < 1$.

6.2. *Viscous corrections to inviscid eigenmodes in cylinders or rectangles*

In a cylinder whose axis is oriented along the rotation axis or in a rectangle whose faces are either parallel or perpendicular to this axis, a complete set of inviscid, regular eigenmodes exists. For these geometries, there is a single singular direction originating from each wedge, and all cases satisfy $|K_1/K_2| = 1$. Consequently, no singular inviscid eigenfunction is associated with any wedge, as the minimal value of α is always $\alpha_1^{(1)} = 2$.

However, viscous corrections could, in principle, exhibit a singular structure originating from the wedges. We argue that this occurs when the boundary layer flow around the wedge possesses a non-zero inward/outward flux. In such cases, this flux must be balanced by a corresponding flux in the bulk, which is described by a Dirac solution.

This phenomenon is clearly illustrated by the configuration analysed in Lin & Kerswell (2024). Their study demonstrates that viscous corrections to the inviscid eigenmode they

consider generate a similar beam structure originating from top and bottom corners when either no-slip or diffusion-free boundary conditions are imposed. In contrast, no such localized structure is observed under stress-free boundary conditions. This difference arises because the boundary layer flux is non-zero for the first two types of boundary conditions, whereas it vanishes for stress-free boundary conditions. Furthermore, when the flux is non-zero, the bulk solution corresponds to a Dirac eigenmode, which accounts for the identical beam structure observed under both no-slip or diffusion-free boundary conditions.

6.3. *Wave beams emitted from the edges of a cube*

The wave field obtained in a rotating tilted cube subjected to libration or precession has been studied in numerous recent works (Wu *et al.*, 2020, 2022, 2024). In this geometry, there are 12 wedges associated with its 12 edges. Along each wedge, the geometry matches that considered in the present paper. Although the edges are finite, we can still analyse the structure of solutions under the assumption of invariance along each edge. Since a cube is a bounded volume, the results of the present paper apply only if the rays emitted from an edge do not return to the same edge. We believe that this condition is not restrictive: rays emitted from one edge typically terminate at an attractor in the bulk or at an attracting edge that does not emit rays, as in the case of Greenspan's triangle.

For both libration and precession forcing, the normal velocity on the cube faces is non-zero. Thus, we are dealing with an inviscid forcing, and we can focus on the inviscid singular eigensolutions associated with each wedge.

To obtain waves that are independent of the edge coordinate, the plane perpendicular to the edge must intersect the double-cone of possible wavevectors. If the angle of this cone is $\theta = \mathrm{acos}(\omega)$ (with $0 \leq \theta \leq \pi/2$, and ω non-dimensionalized by 2Ω), then the angle β ($0 \leq \beta \leq \pi/2$) which defines the orientation of this plane with respect to the rotation axis [see figure 1(a)], must satisfy the condition $\beta < \theta$. When this condition holds, the intersections define four possible wavevectors, from which the directions of wave propagation can be deduced. In the plane perpendicular to the edge, these wavevectors form angles θ_c, $-\theta_c$, $\pi - \theta_c$, and $\pi + \theta_c$ with respect to the projection of the rotation axis in this plane, where $\cos\theta_c = (\cos\theta)/(\cos\beta)$. The directions of propagation, being perpendicular to the wavevectors make angles $\pi/2-\theta_c$, $\pi/2+\theta_c$, $3\pi/2-\theta_c$, and $3\pi/2+\theta_c$ with respect to that projected axis.

In a cube, the edges can be grouped by 4 with the same orientation direction. The four wedges obtained from these edges in the plane perpendicular to the edge direction form a partition of the plane into four right-angle sectors as illustrated in figure 13. Each wedge can then contain zero, one or two singular directions of wave emission, but the total of these directions is always 4 for the four wedges.

Two inclined configurations have been studied by Wu *et al.* (2020, 2022, 2024):

• **Case 1**: The rotation axis is along the large diagonal connecting two opposite vertices (Wu *et al.*, 2020, 2024). In this case, all the edges are such that $\beta = \mathrm{acos}(\sqrt{2/3})$. For a given edge direction, the four associated wedges form, in the plane perpendicular to the edge direction, the configuration illustrated in figure 13(a). The angle θ_c is defined in this case by $\theta_c = \mathrm{acos}(\sqrt{3/2}\,\omega)$. From this figure, we immediately deduce that

  ◦ $0 < \omega < 1/\sqrt{3}$: North and South wedges do not contain singular directions: these edges are attracting edges. East and West wedges possess two singular directions.

  ◦ $1/\sqrt{3} < \omega < \sqrt{2/3}$: The situation is reversed. North and South wedges possess two singular directions while East and West wedges do not contain singular directions.

  ◦ $\sqrt{2/3} < \omega < 1$: No waves independent of the edge coordinate exist.

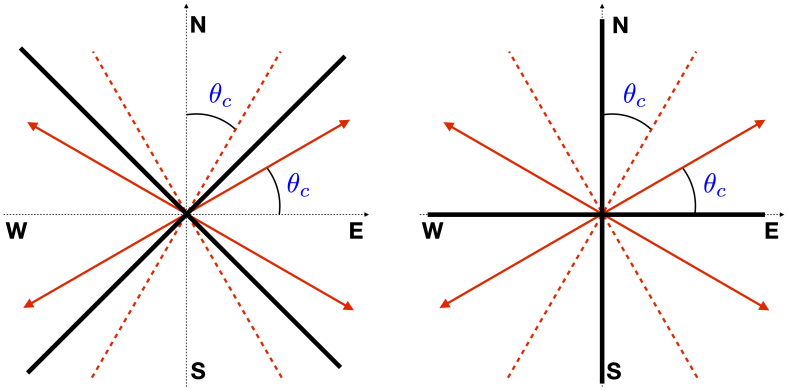

FIGURE 13. Wedge geometry in a cube for cases 1 and 2: cross section in the plane perpendicular to an edge direction. The four wedges associated with a same edge direction are shown in black solid lines on the same plot with the edge in the center. They partition the plane in four right-angle sectors. The red dotted lines indicate the directions of the wavevectors while the red solid lines indicate the singular directions of propagation. (a) The boundaries are inclined at $\pi/4$. This situation corresponds to all the wedges of case 1, and to the 4 wedges associated with the edges perpendicular to the rotation axis in case 2. (b) The boundaries are horizontal and vertical in the plane perpendicular to the edge. This situation corresponds to the 8 other wedges of case 2.

• **Case 2**: The rotation axis passes through the middle of two opposite edges (Wu *et al.*, 2022). In this case, four edges are horizontal ($\beta = 0$), while the other 8 satisfy $\beta = \pi/4$. For the four horizontal edges, the wedge geometry in the plane perpendicular to the edge direction is as in case 1 [figure 13(a)] but θ_c is now defined by $\theta_c = \mathrm{acos}(\omega)$. For the 8 other edges, the wedge geometry is different as illustrated in figure 13(b). In this case, $\theta_c = \mathrm{acos}(\sqrt{2}\,\omega)$. From these two figures, we obtain that
  - $0 < \omega < 1/\sqrt{2}$: North and South "horizontal" wedges are attracting, while East and West horizontal wedges possess two singular directions; all the other wedges has a single direction of emission. However, for those wedges, because $\alpha_1^{(1)} = 2$, there is no singularity along this direction.
  - $1/\sqrt{2} < \omega < 1$: East and West "horizontal" wedges become attracting, while North and and South horizontal wedges now possess two singular directions. There are no wave along the other wedges.

Wu *et al.* (2020) observed that wave sheet structures are emitted from the edges and proposed a rule based on symmetry arguments to determine their directions of propagation. Wu *et al.* (2022) later proposed an alternative prescription, requiring the wave sheet to be tangent to the cone of waves emitted from the vertices. They argued that this prescription aligns more closely with numerical results than the initial rule. Importantly, this prescription does not rely on specific symmetry conditions and is consistent with the singular directions obtained in the present study. As demonstrated in Wu *et al.* (2024), this second rule implies that the normal to the cone in the selected direction is orthogonal to the edge direction. Since this normal is parallel to the wavector associated with the propagation direction, this condition reduces to our own: the wavevector is in the plane perpendicular to the edge, or equivalently, the wave emitted from the edge is independent of the edge coordinate.

Wu *et al.* (2022) and Wu *et al.* (2024) further showed that the location of these wave sheets is in agreement with local extrema of vorticity in numerical simulation, strongly suggesting that singular inviscid eigenmodes are indeed excited.

The present theory adds several new insights:
- It provides the index of the singularity, from which we derived a viscous approximation for the sheet structure. This paves the way for quantitative comparison with numerical solutions.
- It explains why identical sheet structures are observed for both libration and precession forcing, as they correspond to homogeneous solutions (eigenmodes) without external forcing.
- It explains why sheets are visible for certain wedges and not for others. Specifically we demonstrated that vertical right-angle wedges, such as those in case 2 of figure 13(b), exhibit no singularity along the direction of emission.
- It offers a simpler method to identify the role of each edge (attracting, singular wave emission, or no wave) and to determine both the emission direction of singular waves and their strength.

Wu *et al.* (2020, 2022, 2024) also noted that vertices act as sources of waves, exhibiting the conical structure expected from point-wise excitation. It would be valuable to investigate whether these structures are associated with an inviscid singularity and to characterize their properties.

7. Conclusion

In this study, we have investigated, within a general framework, the effect of a 2D wedge on the structure of a harmonic inertial wave field. We have demonstrated that inviscid singularities are generically generated in the presence of a wedge, provided the domain contains at least one characteristic emanating from the apex. These singularities correspond to singular eigenmodes, that satisfy homogeneous boundary conditions on the wedge and outward wave conditions at infinity. They manifest as a velocity field that diverges as $|x_\perp|^{\alpha-1}$ when approaching one of the characteristic directions emanating from the wedge apex. We have also shown that the possible complex exponents α are given by a simple discrete expression [see equation (3.26)], which depends solely on the two wedge angles and the wave propagation angle. We have argued that the exponent with the smallest real part, such that $\Re e(\alpha) \geq 1/2$ to ensure finite energy, is in general selected in the case of an inviscid forcing.

Furthermore, we have explained how a viscous approximation can be constructed from the inviscid singularity. This approximation extends the self-similar expression first derived by Moore & Saffman (1969) to complex singularity indices. It describes the transverse structure localized around the singular direction and how its amplitude and width vary as the wave beam travels away from the wedge apex. The next-order correction to this solution, accounting for the enforcement of the no-slip boundary condition, has also been calculated.

Finally viscous forcing has been considered. We have shown that although the boundary layer flow does not induce Ekman pumping, it generally produces a tangential flow mismatch on both sides of the wedge. We have argued that this mismatch must be balanced by a radial flux in the bulk, which fully prescribes the amplitude of the Dirac eigenmode (the only singular eigenmode exhibiting a radial flux). A complete viscous approximation of the solution, without adjustable parameters, has then been obtained.

The theoretical predictions have been tested against direct numerical simulation results for both inviscid and viscous forcing. For inviscid forcing, we have considered a vertically oscillating inclined square in an unbounded domain. We have shown that the theory almost perfectly reproduces the complex structure of the linear harmonic solution near

each wedge. The same geometry has been considered with a transverse oscillation, giving rise to viscous forcing. We have shown that for the wedges exhibiting a tangential flux mismatch, the Dirac eigenmode is indeed excited with the amplitude and phase predicted by the theory. For the other wedges, for which there is no tangential flux mismatch, the weak response observed in the bulk has also been shown to correspond to a singular eigenmode.

A viscous forcing of the flow in a bounded geometry (Greenspan's triangle) has also been simulated and shown to be very well predicted by the present theory, demonstrating that the unbounded domain hypothesis may not be necessary. We suspect that the only requirement is that the rays emitted from the apex of the wedge do not return to the wedge after reflections on the domain boundaries.

A few application and extensions of the results have been proposed. In particular, the present theory immediately predicts that the scattering of plane wave by a sharp wedge should in general contain both a diffracted and back-refracted wave components that cannot be captured by classical ray theory. Although the analysis has been limited to 2D wedges, we suspect that it could also be extented to 3D configurations. We have argued that the viscous correction to a 3D inviscid linear global mode in a cylinder could be dominated by a Dirac eigenmode emitted from its corners when there is a tangential flow mismatch in the boundary layer at these points. Finally, we have shown that the present theory could potentially explain the observation of the sheet-like structures emitted from certain edges in librating or precessing tilted cubes.

Declaration of Interests. The authors report no conflict of interest.

Appendix A. Stokes boundary layer flow

We provide here the linear viscous flow generated by (small) tangential or transverse oscillations of the plane $\mathcal{P}_1$. We define the normal vector $\mathbf{e}_n$ to this plane towards the fluid, the tangential vector $\mathbf{e}_t = \mathbf{e}_y \times \mathbf{e}_n$ and introduce spatial coordinates x_t and x_n along $\mathbf{e}_t$ and $\mathbf{e}_n$

$$x_t = \cos\theta_1 x + \sin\theta_1 z \ , \quad x_n = -\sin\theta_1 x + \cos\theta_1 z, \tag{A 1a}$$

$$\mathbf{e}_t = \cos\theta_1 \mathbf{e}_x + \sin\theta_1 \mathbf{e}_z \ , \quad \mathbf{e}_n = -\sin\theta_1 \mathbf{e}_x + \cos\theta_1 \mathbf{e}_z. \tag{A 1b}$$

In the frame $(\mathbf{e}_t, \mathbf{e}_y, \mathbf{e}_n)$, the governing equations for the velocity and pressure amplitudes (u_t, u_y, u_n, p) of a flow, oscillating at the frequency $\omega = f\cos\theta_c$ and independent of the y variable, are

$$-\mathrm{i}\cos\theta_c u_t + \tan\beta\, u_n - \cos\theta_1\, u_y = -\frac{\partial p}{\partial x_t} + E\nabla^2 u_t, \tag{A 2a}$$

$$-\mathrm{i}\cos\theta_c u_y + \cos\theta_1\, u_t - \sin\theta_1\, u_n = E\nabla^2 u_y, \tag{A 2b}$$

$$-\mathrm{i}\cos\theta_c u_n + \sin\theta_1\, u_y - \tan\beta\, u_t = -\frac{\partial p}{\partial x_n} + E\nabla^2 u_n, \tag{A 2c}$$

$$\frac{\partial u_t}{\partial x_t} + \frac{\partial u_n}{\partial x_n} = 0, \tag{A 2d}$$

where we have non-dimensionalized spatial and temporal variables by a spatial scale l and the Coriolis parameter f respectively and defined

$$E = \frac{\nu}{f l^2} \ . \tag{A 3}$$

The boundary conditions are

$$\mathbf{u}(x_n = 0) = U_t \mathbf{e}_t + U_y \mathbf{e}_y, \tag{A 4}$$

where $U_t(x_t)$ and $U_y(x_t)$ could, in principle, be functions of x_t.

Introducing the viscous scale $\eta = x_n/\sqrt{E}$ and the viscous ansatz

$$(u_t, u_y, u_n, p) = (u_t^{(0)}, u_y^{(0)}, \sqrt{E}u_n^{(1)}, \sqrt{E}p^{(1)}), \tag{A 5}$$

we obtain

$$-\mathrm{i}\cos\theta_c u_t^{(0)} - \cos\theta_1 u_y^{(0)} = \frac{\partial^2 u_t^{(0)}}{\partial\eta^2}, \tag{A 6a}$$

$$-\mathrm{i}\cos\theta_c u_y^{(0)} + \cos\theta_1 u_t^{(0)} = \frac{\partial^2 u_y^{(0)}}{\partial\eta^2}, \tag{A 6b}$$

$$\sin\theta_1 u_y^{(0)} - \tan\beta\, u_t^{(0)} = \frac{\partial p^{(1)}}{\partial\eta}, \tag{A 6c}$$

$$\frac{\partial u_t^{(0)}}{\partial x_t} + \frac{\partial u_n^{(1)}}{\partial\eta} = 0. \tag{A 6d}$$

From these equations, we immediately get that $u_t^{(0)}$ and $u_y^{(0)}$ satisfy the same equation

$$\left(\frac{\partial^2}{\partial\eta^2} + \mathrm{i}\cos\theta_c\right)^2 u_t^{(0)} + \cos^2\theta_1 u_t^{(0)} = 0. \tag{A 7}$$

The solution should vanish away from the boundary so we can write

$$u_t^{(0)} = C_1^+ e^{-\lambda_1^+\eta} + C_1^- e^{-\lambda_1^-\eta}, \tag{A 8}$$

where $\lambda_1^\pm$ are roots of

$$(\lambda_1^\pm)^2 = -\mathrm{i}(\cos\theta_c \pm \cos\theta_1), \tag{A 9}$$

satisfying $\Re e(\lambda_1^\pm) > 0$. This leads to the following expressions

$$\lambda_1^\pm = \begin{cases} e^{-\mathrm{i}\pi/4}\sqrt{\cos\theta_c \pm \cos\theta_1} & \text{if} \quad \cos\theta_c \pm \cos\theta_1 > 0, \\ e^{\mathrm{i}\pi/4}\sqrt{|\cos\theta_c \pm \cos\theta_1|} & \text{if} \quad \cos\theta_c \pm \cos\theta_1 < 0, \end{cases} \tag{A 10}$$

Using (A 6a), we also get

$$u_y^{(0)} = \mathrm{i}\left(C_1^+ e^{-\lambda_1^+\eta} - C_1^- e^{-\lambda_1^-\eta}\right). \tag{A 11}$$

The boundary condition (A 4) gives a linear system for $C_1^\pm$ which is immediately solved as

$$C_1^\pm = \frac{U_t \mp \mathrm{i}U_y}{2}\ . \tag{A 12}$$

Equation (A 6d) gives the normal velocity

$$u_n^{(1)} = -\frac{\partial C_1^+}{\partial x_t}\frac{1 - e^{-\lambda_1^+\eta}}{\lambda_1^+} - \frac{\partial C_1^-}{\partial x_t}\frac{1 - e^{-\lambda_1^-\eta}}{\lambda_1^-}. \tag{A 13}$$

When the oscillating forcing of the boundary is independent of x_t (U_t and U_y are constants), this equation reduces to $u_n^{(1)} = 0$. This means no Ekman pumping. No forcing of a solution in the bulk is therefore expected in that case.

Note however that in that case a velocity flux along the boundary is nevertheless

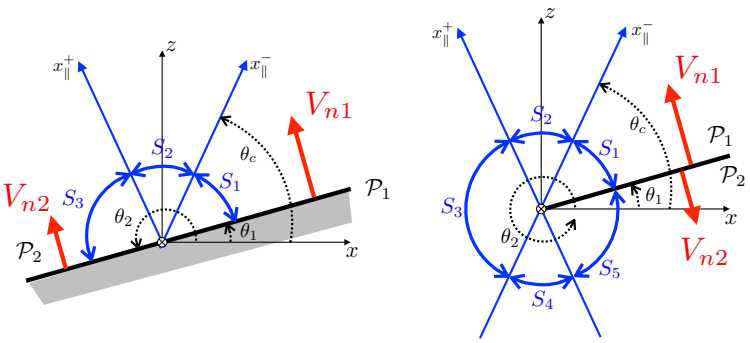

(a) (b)

FIGURE 14. Configurations where a singular forced response is obtained. (a) Planar geometry ($\theta_2 = \theta_1 + \pi$) with $V_{n1} \neq V_{n2}$, (b) Knife-edge geometry ($\theta_2 = \theta_1 + 2\pi$) with $V_{n2} \neq -V_{n1}$.

present and given in the direction $\mathbf{e}_t$ (for an unitary transverse distance) by

$$F_{t1} = \int_0^\infty u_t dx_n = \sqrt{E}\int_0^\infty u_t^{(0)}(\eta)d\eta = \sqrt{E}\left(\frac{C_1^+}{\lambda_1^+} + \frac{C_1^-}{\lambda_1^-}\right). \tag{A 14}$$

When U_t or U_y are functions of x_t, a normal component $u_n^{(1)}$ is generated that will in general force a response in the bulk. We have seen that inviscid eigenfunctions with a velocity field of the form $a_j|x_\perp^+|^{\alpha-1} + b_j|x_\perp^-|^{\alpha-1}$ exist. These solutions have a tangential and transverse velocity of the form $|x_t|^{\alpha-1}$ on $\mathcal{P}_1$ and $\mathcal{P}_2$. To cancel these velocities, a opposite flow should be added in the boundary layer. More precisely if on $\mathcal{P}_1$, we have

$$U_t = a_1|x_t|^{\alpha-1}\ , \quad U_y = b_1|x_t|^{\alpha-1} \tag{A 15}$$

then equation (A 13) gives

$$u_n^{(1)} = \frac{(1-\alpha)|x_t|^{\alpha-2}}{2}\left((a_1 - \mathrm{i}b_1)\frac{1-e^{-\lambda_1^+\eta}}{\lambda_1^+} + (a_1 + \mathrm{i}b_1)\frac{1-e^{-\lambda_1^-\eta}}{\lambda_1^-}\right). \tag{A 16}$$

This induces an Ekman pumping in the bulk given by

$$U_{\text{Ekman}} = \sqrt{E}\lim_{\eta\to+\infty} u_n^{(1)} = \sqrt{E}\frac{(1-\alpha)|x_t|^{\alpha-2}}{2}\left(\frac{a_1 - \mathrm{i}b_1}{\lambda_1^+} + \frac{a_1 + \mathrm{i}b_1}{\lambda_1^-}\right). \tag{A 17}$$

Appendix B. Singular inviscid forced response

In section §3.2, we have seen that a regular forced response is not obtained if $\theta_2 = \theta_1 + \pi$ and $V_{n1} \neq V_{n2}$ or if $\theta_2 = \theta_1 + 2\pi$ and $V_{n1} \neq -V_{n2}$. In this section, we show that, in those cases, the forced response takes a different form with a logarithmic singularity.

B.1. *Planar geometry ($\theta_2 = \theta_1 + \pi$)*

This case corresponds to the situation illustrated in figure 14(a).

In that case, $K_1 = K_2$, see equation (2.10). We search solutions in S_1 in the form

$$\left.\begin{aligned} u_\parallel^- &\sim B^- + A^-\log|x_\perp^-| \\ u_\parallel^+ &\sim B^+ + A^+\log|x_\perp^+| \end{aligned}\right\} \text{for}\ \ \mathbf{x}\in S_1. \tag{B 1}$$

The condition of radiation given in section 3.1 imposes that

$$\left.\begin{aligned} u_\parallel^- &\sim B^- + A^-(\log|x_\perp^-| - \mathrm{i}\pi) \\ u_\parallel^+ &\sim B^+ + A^+ \log|x_\perp^+|, \end{aligned}\right\} \text{for } \ \mathbf{x} \in S_2 \tag{B 2}$$

$$\left.\begin{aligned} u_\parallel^- &\sim B^- + A^-(\log|x_\perp^-| - \mathrm{i}\pi) \\ u_\parallel^+ &\sim B^+ + A^+(\log|x_\perp^+| + \mathrm{i}\pi) \end{aligned}\right\} \text{for } \ \mathbf{x} \in S_3. \tag{B 3}$$

If we plug expressions (B 1) in (3.12a) and expressions (B 3) in (3.12b), we first get the condition $A_+ = K_1 A_-$ to cancel the logarithmic terms, and the following linear system to cancel the constant terms

$$B^+ - K_1(A^- \log|K_1| + B^-) = \frac{V_{n1}}{\sin(\theta_1 + \theta_c)}, \tag{B 4a}$$

$$B^+ + \mathrm{i}\pi K_1 A^- - K_1(A^- \log|K_1| - \mathrm{i}\pi A^- + B^-) = \frac{V_{n2}}{\sin(\theta_1 + \theta_c)}. \tag{B 4b}$$

These equations give

$$A^- = \frac{V_{n2} - V_{n1}}{2\mathrm{i}\pi \sin(\theta_1 - \theta_c)}, \tag{B 5a}$$

$$B^+ - K_1 B^- = \frac{(V_{n2} - V_{n1})\log|K_1| + 2\mathrm{i}\pi V_{n1}}{2\mathrm{i}\pi \sin(\theta_1 + \theta_c)}. \tag{B 5b}$$

As in section §3.2, we see that any constant solution $u_\parallel^- = V$ and $u_\parallel^+ = K_1 V$ corresponding to a uniform flow along the boundary can be added without modifying these conditions. Note also that the logarithmic singularity disappears ($A^- = 0$) when $V_{n1} = V_{n2}$, as it was seen at the end of section §3.2.

B.2. *Knife-edge geometry ($\theta_2 = \theta_1 + 2\pi$)*

This case corresponds to the situation illustrated in figure 14(b). It can be treated as the planar geometry. The domain now contains five domains S_j, $j = 1, .., 5$. We can still search a solution of the form (B 1)- (B 3) in the sectors S_1, S_2 and S_3. For the two other sectors, the condition of radiation imposes

$$\left.\begin{aligned} u_\parallel^- &\sim B^- + A^-(\log|x_\perp^-| - 2\mathrm{i}\pi) \\ u_\parallel^+ &\sim B^+ + A^+(\log|x_\perp^+| + \mathrm{i}\pi), \end{aligned}\right\} \text{for } \ \mathbf{x} \in S_4, \tag{B 6}$$

$$\left.\begin{aligned} u_\parallel^- &\sim B^- + A^-(\log|x_\perp^-| - 2\mathrm{i}\pi) \\ u_\parallel^+ &\sim B^+ + A^+(\log|x_\perp^+| + 2\mathrm{i}\pi) \end{aligned}\right\} \text{for } \ \mathbf{x} \in S_5. \tag{B 7}$$

Plugging (B 6) and (B 7) in (3.12a) and (3.12b) respectively gives, as before, $A^+ = K_1 A^-$ to cancel the logarithm terms, and a linear system to cancel the constant terms

$$B^+ - K_1(A^- \log|K_1| + B^-) = \frac{V_{n1}}{\sin(\theta_1 + \theta_c)}, \tag{B 8a}$$

$$B^+ + 2\mathrm{i}\pi K_1 A^- - K_1(A^- \log|K_1| - 2\mathrm{i}\pi A^+ B^-) = -\frac{V_{n2}}{\sin(\theta_1 + \theta_c)}. \tag{B 8b}$$

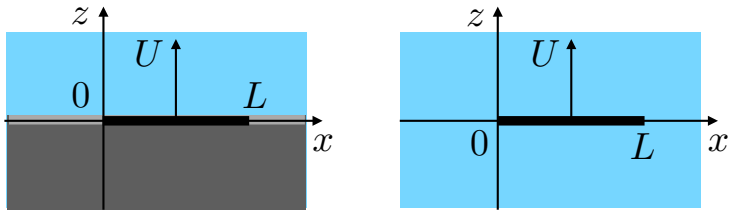

(a) (b)

FIGURE 15. Sketch of the considered geometries. (a) Oscillating velocity flux of amplitude U through a slit of length L in the half-plane $z > 0$; (b) Horizontal barrier of length L vertically oscillating with a velocity amplitude U in the full plane.

The solution of this system is

$$A^- = -\frac{V_{n1} + V_{n2}}{4\mathrm{i}\pi \sin(\theta_1 - \theta_c)}, \tag{B 9a}$$

$$B^+ - K_1 B_- = -\frac{(V_{n1} + V_{n2}) \log|K_1| + 4\mathrm{i}\pi V_{n1}}{4\mathrm{i}\pi \sin(\theta_1 + \theta_c)}. \tag{B 9b}$$

The logarithmic singularity disappears ($A^- = 0$) when $V_{n1} = -V_{n2}$ as expected for this geometry.

Appendix C. Comparison with known inviscid solutions

Global inviscid solutions have been provided in the literature for the two geometries illustrated in figure 15. The objective is to show that we recover the local solution obtained close to each wedge.

C.1. *Oscillating vertical flux from a slit in the upper half-plane* ($z \geq 0$).

The general inviscid solution obtained in the upper half-plane for the streamfunction Ψ from a boundary condition of the form $\Psi(x, z = 0) = \Psi_0(x)$ can formally be written as

$$\Psi(x,z) = \frac{1}{2\pi}\int_{-\infty}^{0} \hat{\Psi}_0(k) e^{\mathrm{i}k(x - \mathrm{ctan}\theta_c z)} dk + \int_{0}^{+\infty} \hat{\Psi}_0(k) e^{\mathrm{i}k(x + \mathrm{ctan}\theta_c z)} dk \tag{C 1}$$

where $\hat{\Psi}_0(k) = \int_{-\infty}^{+\infty} \Psi_0(x) e^{-\mathrm{i}kx} dx$ is the Fourier transform of $\Psi_0(x)$. This expression can also be written as (3.4) with

$$\Psi^-(x_\perp^-) = \frac{1}{2\pi}\int_{-\infty}^{0} \hat{\Psi}_0(k) e^{-\mathrm{i}kx_\perp^-/\sin\theta_c} dk \;;\quad \Psi^+(x_\perp^+) = \frac{1}{2\pi}\int_{0}^{+\infty} \hat{\Psi}_0(k) e^{\mathrm{i}kx_\perp^+/\sin\theta_c} dk. \tag{C 2}$$

Consider for instance Ψ^+. Using the Heaviside function $H(k)$ and its inverse Fourier transform, one can write

$$\begin{aligned}
\Psi^+(x_\perp^+) &= \frac{1}{2\pi}\int_{-\infty}^{\infty} \Psi_0(x) \left(\int_{-\infty}^{+\infty} H(k) e^{\mathrm{i}k(x_\perp^+/\sin\theta_c - x)} dk \right) dx \\
&= \int_{-\infty}^{\infty} \Psi_0(x) \left(\frac{1}{2}\delta(x - x_\perp^+/\sin\theta_c) + \frac{1}{2\pi\mathrm{i}(x - x_\perp^+/\sin\theta_c)} \right) dx \\
&= \frac{1}{2}\Psi_0(x_\perp^+/\sin\theta_c) + \frac{\mathrm{i}}{2}\mathcal{H}(\Psi_0)(x_\perp^+/\sin\theta_c)
\end{aligned}$$

where the Hilbert transform $\mathcal{H}(\Psi_0)$ of Ψ_0 is defined as a Cauchy principal part integral

$$\mathcal{H}(\Psi_0)(x) = \frac{1}{\pi} \fint_{-\infty}^{\infty} \frac{\Psi_0(z)}{x-z} dz \ . \tag{C 3}$$

Similarly, we get

$$\Psi^-(x_\perp^-) = \frac{1}{2}\Psi_0(-x_\perp^-/\sin\theta_c) - \frac{\mathrm{i}}{2}\mathcal{H}(\Psi_0)(-x_\perp^-/\sin\theta_c). \tag{C 4}$$

From these expressions and (3.6a,b), we can deduce the general expression of the velocity fields $u_\parallel^+$ and $u_\parallel^-$:

$$u_\parallel^+ = \frac{1}{2\sin\theta_c}\left(U_0\left(\frac{x_\perp^+}{\sin\theta_c}\right) + \frac{\mathrm{i}}{2}\mathcal{H}(U_0)\left(\frac{x_\perp^+}{\sin\theta_c}\right)\right), \tag{C 5a}$$

$$u_\parallel^- = \frac{1}{2\sin\theta_c}\left(U_0\left(-\frac{x_\perp^-}{\sin\theta_c}\right) - \frac{\mathrm{i}}{2}\mathcal{H}(U_0)\left(-\frac{x_\perp^-}{\sin\theta_c}\right)\right), \tag{C 5b}$$

where $U_0(x) = -\partial_x\Psi_0(x)$ is the vertical velocity on the boundary.

For the forcing considered in section B.1, we have $U_0 = V_{n1}H(x) + V_{n2}H(-x)$. Since

$$\mathcal{H}(H(\square))(x) = \frac{\log|x|}{\pi}$$

we immediately obtain:

$$u_\parallel^+ = \frac{1}{2\sin\theta_c}\left(V_{n1}H(x_\perp^+) + V_{n2}H(-x_\perp^+) + \frac{\mathrm{i}(V_{n1}-V_{n2})}{\pi}\log\left|\frac{x_\perp^+}{\sin\theta_c}\right|\right), \tag{C 6a}$$

$$u_\parallel^- = \frac{1}{2\sin\theta_c}\left(V_{n1}H(-x_\perp^-) + V_{n2}H(x_\perp^-) - \frac{\mathrm{i}(V_{n1}-V_{n2})}{\pi}\log\left|\frac{x_\perp^-}{\sin\theta_c}\right|\right), \tag{C 6b}$$

which exactly corresponds to the expressions (B 1), (B 3), (B 5a,b) of the singular forced solution with $\theta_1 = 0$, $K_1 = -1$ and the choice of the arbitrary constant V such that

$$B^- = V = \frac{V_{n1}}{2\sin\theta_c} + \frac{\mathrm{i}(V_{n1}-V_{n2})}{\pi}\log|\sin\theta_c| \,. \tag{C 7}$$

For a forcing in a finite interval, as illustrated in figure 15(a), such that

$$U_0(x) = U(H(x) - H(x-L)),$$

we obtain

$$u_\parallel^+ = \frac{1}{2\sin\theta_c}\left(U_0\left(\frac{x_\perp^+}{\sin\theta_c}\right) + \frac{\mathrm{i}U}{\pi}\log\left|\frac{x_\perp^+}{x_\perp^+ - L\sin\theta_c}\right|\right), \tag{C 8a}$$

$$u_\parallel^- = \frac{1}{2\sin\theta_c}\left(U_0\left(-\frac{x_\perp^-}{\sin\theta_c}\right) - \frac{\mathrm{i}U}{\pi}\log\left|\frac{x_\perp^-}{x_\perp^- + L\sin\theta_c}\right|\right). \tag{C 8b}$$

For $|x_\perp^\pm| \ll L$, these expressions become

$$u_\parallel^+ \sim \frac{1}{2\sin\theta_c}\left(UH(x_\perp^+) + \frac{\mathrm{i}U}{\pi}\left(\log\left|\frac{x_\perp^+}{L\sin\theta_c}\right| + \frac{x_\perp^+}{L\sin\theta_c}\right)\right) \tag{C 9a}$$

$$u_\parallel^- \sim \frac{1}{2\sin\theta_c}\left(UH(-x_\perp^-) - \frac{\mathrm{i}U}{\pi}\left(\log\left|\frac{x_\perp^-}{L\sin\theta_c}\right| - \frac{x_\perp^-}{L\sin\theta_c}\right)\right). \tag{C 9b}$$

At leading order, we recognize the singular forced solution, and the first eigenmode corresponding to $\alpha_1^{(2)} = 1$ for this case. Higher order terms are associated with eigenmodes with larger $\alpha = \alpha_n^{(2)} = n$, $n = 2, 3, ...$

C.2. *Global solution for a vertically oscillating horizontal barrier*

This configuration is illustrated in figure 15(b). The solution was given by (Voisin, 2021, table 3) for a stratified fluid. The solution in a rotating fluid is just the complex conjugate of this solution. With our notation, it can be written as

$$u_\parallel^- = \frac{U}{2\sin\theta_c}\left(1+\frac{2\tilde{x}_\perp^-}{(4(\tilde{x}_\perp^-)^2-L^2\sin^2\theta_c)^{1/2}}\right), \tag{C 10a}$$

$$u_\parallel^+ = \frac{U}{2\sin\theta_c}\left(1-\frac{2\tilde{x}_\perp^+}{(4(\tilde{x}_\perp^+)^2-L^2\sin^2\theta_c)^{1/2}}\right), \tag{C 10b}$$

where the square root is defined by

$$(4(\tilde{x}_\perp^\pm)^2-L^2\sin^2\theta_c)^{1/2} = |4(\tilde{x}_\perp^\pm)^2-L^2\sin^2\theta_c|^{1/2}\mathrm{sgn}(\tilde{x}_\perp^\pm) \quad (2|\tilde{x}_\perp^\pm|>L\sin\theta_c), \tag{C 11a}$$

$$= \mathrm{i}|4(\tilde{x}_\perp^\pm)^2-L^2\sin^2\theta_c|^{1/2}\mathrm{sgn}(z) \quad (2|\tilde{x}_\perp^\pm|<L\sin\theta_c), \tag{C 11b}$$

and $2\tilde{x}_\perp^\pm = 2x_\perp^\pm \mp L\sin\theta_c$.

If we consider the solution for $|x_\perp^\pm|/L \ll 1$, we obtain the configuration that we have studied above for $\theta_1=0$, $\theta_2=2\pi$, $U_1=-U_2=U$. In this limit, the above expressions become up to $O(\sqrt{|x_\perp^\pm|/L})$ terms

$$u_\parallel^- \sim \frac{U}{2\sin\theta_c} + U\sqrt{\frac{L}{\sin\theta_c|x_\perp^-|}}\times\begin{cases}1 & (x_\perp^->0)\\ -\mathrm{i}\,\mathrm{sgn}(z) & (x_\perp^-<0)\end{cases} \tag{C 12a}$$

$$u_\parallel^+ \sim \frac{U}{2\sin\theta_c} - U\sqrt{\frac{L}{\sin\theta_c|x_\perp^+|}}\times\begin{cases}\mathrm{i}\,\mathrm{sgn}(z) & (x_\perp^+>0)\\ 1 & (x_\perp^+<0)\end{cases} \tag{C 12b}$$

We recognize in the first term the regular forced response (3.14) with $V=U/2$. The second term corresponds to a singular eigenmode of index $\alpha=1/2$ corresponding to (3.24) with $n=1$.

References

Abramowitz, M. & Stegun, I. A. 1965 *Handbook of Mathematical Functions*. New York: Dover.

Baines, P. G. 1971 The reflexion of internal/inertial waves from bumpy surfaces. *J. Fluid Mech.* **46**, 273–291.

Bardakov, R. N., Vasil'ev, A. Y. & Chashechkin, Y. D. 2007 Calculation and measurement of conical beams of three-dimensional periodic internal waves excited by a vertically oscillating piston. *Fluid Dyn.* **42**, 612–626.

Beardsley, R. C. 1970 An experimental study of inertial waves in a closed cone. *Stud. Appl. Math.* **49**, 187–196.

Bell, T. H. 1975 Topographically generated internal waves in the open ocean. *J. Geophys. Res.* **80**, 320–327.

Boisson, J., Lamriben, C., Maas, L. R. M., Cortet, P. P. & Moisy, F. 2012 Inertial waves and modes excited by the libration of a rotating cube. *Phys. Fluids* **24**, 076602.

Chang, X., He, J., Favier, B. & Le Dizès, S. 2026 Zonal flows driven by libration in rotating spherical shells: the case of periodic characteristic paths. *J. Fluid Mech.* **1026**, A15.

Davis, A. M. J. & Llewellyn Smith, S. G. 2010 Tangential oscillations of a circular disk in a viscous stratified fluid. *J. Fluid Mech.* **656**, 342–359.

Deville, M. O., Fischer, P. F. & Mund, E. H. 2002 *High-Order Methods for Incompressible Fluid Flow*. Cambridge University Press.

Fischer, P. F. 1997 An overlapping Schwarz method for spectral element solution of the incompressible Navier-Stokes equations. *Journal of Computational Physics* **133**, 84–101.

Greenspan, H. P. 1968 *The theory of rotating fluids*. Cambridge University Press.

Greenspan, H. P. 1969 On the inviscid theory of rotating fluids. *Stud. Appl. Math.* **48**, 10–28.

He, J., Favier, B., Rieutord, M. & Le Dizès, S. 2022 Internal shear layers in librating spherical shells: the case of periodic characteristic paths. *J. Fluid Mech.* **939**, A3.

He, J., Favier, B., Rieutord, M. & Le Dizès, S. 2023 Internal shear layers in librating spherical shells: the case of attractors. *J. Fluid Mech.* **974**, A3.

Hurley, D. G. 1970 Internal waves in a wedge-shaped region. *J. Fluid Mech.* **43**, 97–120.

Hurley, D. G. 1972 A general method for solving steady-state internal gravity wave problems. *J. Fluid Mech.* **56**, 721–740.

Hurley, D. G. 1997 The generation of internal waves by vibrating elliptic cylinders. Part 1. Inviscid solution. *J. Fluid Mech.* **351**, 105–118.

Il'inyhk, Y. S. & Chashechkin, Y. D. 2004 Generation of periodic motions by a disk performing torsional oscillations in a viscous, continuously stratified fluid. *Fluid Dyn.* **39**, 148–161.

Kerswell, R. 1995 On the internal shear layers spawned by the critical regions in oscillatory Ekman boundary layers. *J. Fluid Mech.* **298**, 311–325.

Kistovich, Y. V. & Chashechkin, Y. D. 1999 An exact solution of a linearized problem of the radiation of monochromatic internal waves in a viscous fluid. *J. Appl. Math. Mech.* **63**, 587–594.

Klein, M., Seelig, T., Kurgansky, M., Ghasemi, A. V. *et al.* 2014 Inertial wave excitation and focusing in a liquid bounded by a frustrum and a cylinder. *J. Fluid Mech.* **751**, 255–297.

Le Dizès, S. 2015 Wave field and zonal flow of a librating disk. *J. Fluid Mech.* **782**, 178–208.

Le Dizès, S. 2020 Reflection of oscillating internal shear layers: nonlinear corrections. *J. Fluid Mech.* **899**, A21.

Le Dizès, S. 2024 Critical slope singularities in rotating and stratified fluids. *Phys. Rev. Fluids* **9**, 034803.

Le Dizès, S. & Favier, B. 2026 Concentrated beams in differentially rotating and stratified fluids and their reflection at a turning point. *J. Fluid Mech.* **1030**, A35.

Le Dizès, S. & Le Bars, M. 2017 Internal shear layers from librating objects. *J. Fluid Mech.* **826**, 653–675.

Lighthill, M. J. 1978 *Waves in fluids*. Cambridge University Press.

Lin, Y. & Kerswell, R. R. 2024 Weakening the effect of boundaries: "diffusion-free" boundary conditions as a "do least harm" alternative to neumann. *Geo. Astro. Fluid Dyn.* pp. 1–25.

Llewellyn Smith, S. G. & Young, W. R. 2003 Tidal conversion at a very steep ridge. *J. Fluid Mech.* **495**, 175–191.

Maas, L. R. M., Benielli, D., Sommeria, J. & Lam, F.-P. A. 1997 Observation of an internal wave attractor in a confined, stably stratified fluid. *Nature* **388**, 557–561.

Martin, P. A. & Llewellyn Smith, S. G. 2011 Generation of internal gravity waves by an oscillating horizontal disc. *Proc. R. Soc. A* **467**, 3406–3423.

McEwan, A. D. 1970 Inertial oscillations in a rotating fluid cylinder. *J. Fluid Mech.*

40, 603–640.

Moore, D. W. & Saffman, P. G. 1969 The structure of free vertical shear layers in a rotating fluid and the motion produced by a slowly rising body. *Phil. Trans. R. Soc.* A **264**, 597–634.

Mowbray, D. E. & Rarity, B. S. H. 1967 A theoretical and experimental investigation of the phase configuration of internal waves of small amplitude in a density stratified liquid. *J. Fluid Mech.* **28**, 1–16.

Phillips, O. M. 1966 *The Dynamics of the Upper Ocean*. Cambridge University Press.

Robinson, R. M. 1969 The effects of a vertical barrier on internal waves. *Deep-Sea Research* **16**, 421–429.

Robinson, R. M. 1970 The effects of a corner on a propagating internal gravity wave. *J. Fluid Mech.* **42**, 257–267.

St Laurent, L., Stringer, S., Garrett, C. & Perrault-Joncas, D. 2003 The generation of internal tides at abrupt topography. *Deep-Sea Res. I* **50**, 987–1003.

Tanzosh, J. P. & Stone, H. A. 1995 Transverse motion of a disk through a rotating viscous fluid. *J. Fluid Mech.* **301**, 295–324.

Thomas, N. H. & Stevenson, T. N. 1972 A similarity solution for viscous internal waves. *J. Fluid Mech.* **54**, 495–506.

Troitskaya, S. D. 2010 Solution properties of a model problem on oscillations of a rotating fluid in domains with angular points. *Moscow Univ. Phys. Bull.* **65**, 446–453.

Voisin, B. 2003 Limit states of internal wave beams. *J. Fluid Mech.* **496**, 243–293.

Voisin, B. 2021 Boundary integrals for oscillating bodies in stratified fluids. *J. Fluid Mech.* **927**, A3.

Wu, K., Welfert, B. D. & Lopez, J. M. 2020 Reflections and focusing of inertial waves in a librating cube with the rotation axis oblique to its faces. *J. Fluid Mech.* **896**, A5.

Wu, K., Welfert, B. D. & Lopez, J. M. 2022 Reflections and focusing of inertial waves in a tilted librating cube. *J. Fluid Mech.* **947**, A10.

Wu, K., Welfert, B. D. & Lopez, J. M. 2024 Comparison of libration- and precession-driven flows: From linear responses to broadband dynamics. *Fluids* **9**, 151.

Wunsch, C. 1968 On the propagation of internal waves up a slope. *Deep-Sea Research* **15**, 251–258.

Wunsch, C. 1969 Progressive internal waves on slopes. *J. Fluid Mech.* **35**, 131–144.